

Article

# High-Fidelity Image Transmission in Quantum Communication with Frequency Domain Multi-Qubit Techniques

Udara Jayasinghe , Thanuj Fernando  and Anil Fernando \* 

Department of Computer and Information Sciences, University of Strathclyde, Glasgow G1 1XQ, UK; udara.jayasinghe-mudalige@strath.ac.uk (U.J.); thanuj.fernando.2023@uni.strath.ac.uk (T.F.)

\* Correspondence: anil.fernando@strath.ac.uk

## Abstract

This paper proposes a novel quantum image transmission framework to address the limitations of existing single-qubit time domain systems, which struggle with noise resilience and scalability. The framework integrates frequency domain processing with multi-qubit (1 to 8 qubits) encoding to enhance robustness against quantum noise. Initially, images are source-coded using JPEG and HEIF formats with rate adjustment to ensure consistent bandwidth usage. The resulting bitstreams are channel-encoded and mapped to multi-qubit quantum states. These states are transformed into the frequency domain via the quantum Fourier transform (QFT) for transmission. At the receiver, the inverse QFT recovers the time domain states, followed by multi-qubit decoding, channel decoding, and source decoding to reconstruct the image. Performance is evaluated using bit error rate (BER), peak signal-to-noise ratio (PSNR), structural similarity index measure (SSIM), and universal quality index (UQI). Results show that increasing the number of qubits enhances image quality and noise robustness, albeit at the cost of increased system complexity. Compared to time domain processing, the frequency domain approach achieves superior performance across all qubit configurations, with the eight-qubit system delivering up to a 4 dB maximum channel SNR gain for both JPEG and HEIF images. Although single-qubit systems benefit less from frequency domain encoding due to limited representational capacity, the overall framework demonstrates strong potential for scalable and noise-robust quantum image transmission in future quantum communication networks.



Academic Editor: Frank Werner

Received: 12 July 2025

Revised: 1 August 2025

Accepted: 7 August 2025

Published: 11 August 2025

**Citation:** Jayasinghe, U.; Fernando, T.; Fernando, A. High-Fidelity Image Transmission in Quantum Communication with Frequency Domain Multi-Qubit Techniques. *Algorithms* **2025**, *18*, 501. <https://doi.org/10.3390/a18080501>

**Copyright:** © 2025 by the authors. Licensee MDPI, Basel, Switzerland. This article is an open access article distributed under the terms and conditions of the Creative Commons Attribution (CC BY) license (<https://creativecommons.org/licenses/by/4.0/>).

**Keywords:** multi-qubit encoding; quantum communication; quantum frequency domain; QFT; quantum superposition

## 1. Introduction

In today's digitally interconnected world, image transmission serves as a critical enabler for a wide range of intelligent systems and communication technologies. Applications such as high-precision medical diagnostics, automated industrial inspection, smart city surveillance, and immersive augmented reality (AR) [1] rely on the timely and accurate delivery of visual data. As the demand for ultra-high-resolution images and interactive content continues to grow, existing communication infrastructures face mounting pressure due to bandwidth limitations, channel noise, and stringent latency requirements. These constraints are especially severe in real-time or resource-constrained environments, where preserving image fidelity is essential for accurate decision-making and user experience.

In response, classical communication systems have long relied on well-established image compression standards, such as joint photographic experts group (JPEG), high effi-

ciency image format (HEIF), and wavelet-based codecs, together with powerful channel coding schemes such as polar codes, low-density parity check (LDPC), and turbo codes. These techniques, rooted in Shannon's information theory [2], have successfully supported image delivery across a variety of platforms, including the Internet and mobile and satellite networks. However, as the volume and complexity of visual content continue to escalate, these classical methods are increasingly reaching their performance limits. This is particularly evident in compressed image transmission, where inherent compressed data correlations intensify the effects of compression artifacts and make the system more vulnerable to error propagation and visual degradation under noisy channel conditions. As a result, maintaining high perceptual quality while meeting bandwidth and latency constraints is becoming increasingly difficult, underscoring the urgent need for alternative transmission frameworks tailored to modern visual data demands. These fundamental limitations highlight the necessity of exploring new paradigms that transcend classical boundaries, offering enhanced noise resilience, bandwidth efficiency, and scalability for high-fidelity image transmission in next-generation communication systems.

The arrival of next-generation wireless standards, such as 6G and beyond, aims to address some of these concerns through enhanced spectral efficiency and network densification. However, even these advances struggle to meet the extreme requirements of real-time high-fidelity image transmission in dynamic, noisy, or bandwidth-limited environments. These limitations underscore the urgent need for alternative communication paradigms that can operate beyond classical constraints, opening the door to quantum communication.

Quantum communication [3] represents a paradigm shift by harnessing the principles of quantum mechanics, particularly superposition [4], and entanglement [5] to encode, transmit, and decode information. Unlike classical bits, which are binary and sequential, quantum bits (qubits) can represent and process multiple states simultaneously, allowing exponentially more information to be represented with fewer physical resources. This intrinsic parallelism enables not only higher data throughput, but also increased robustness to noise and interference, making quantum communication especially attractive for transmitting complex, high-dimensional data such as images.

Although recent studies have demonstrated the feasibility of quantum-based image transmission using simple time domain quantum communication models [6], these approaches often lack scalability and noise resilience in practical settings. In particular, most of these systems rely on single-qubit encoding, where individual bits are mapped to quantum states one by one, a method that struggles under noisy channels. To address this, multi-qubit encoding has emerged as a promising direction, allowing multiple bits to be simultaneously represented in composite quantum states that exploit the higher dimensionality of the Hilbert space. These multi-qubit states inherently support greater expressiveness and better error resilience, thereby increasing resilience to localized disturbances and noise.

Moreover, many existing studies have yet to fully exploit multi-qubit encoding for quantum image transmission, thereby overlooking the immense potential of utilizing the high-dimensional Hilbert space for media transmission. By encoding information across multiple qubits, quantum systems can represent data within exponentially larger state spaces, enabling more efficient representation and processing of complex image information. This high-dimensional encoding allows concentrating most of the relevant information of an image into fewer quantum states, potentially improving noise resilience and transmission efficiency compared to single-qubit approaches.

In addition to the benefits provided by multi-qubit encoding, operating in the frequency domain introduces further advantages for quantum image transmission. Representing images in the frequency domain allows vital visual information to be concentrated into fewer coefficients, inherently improving resilience to noise and channel degradation.

The quantum Fourier transform (QFT) [7] plays a central role in this approach by providing an efficient means of transforming quantum states from the time domain to the frequency domain. While the theoretical strengths of frequency domain processing are well-established, prior studies have not yet explored its combination with multi-qubit encoding in the context of image transmission. This unexplored integration has the potential to leverage both the expanded Hilbert space and the noise-mitigating nature of frequency domain representations, paving the way for more robust and efficient quantum image communication systems.

To bridge these gaps, this paper introduces a novel quantum communication framework for image transmission that combines multi-qubit encoding with the quantum frequency domain using the QFT. In the proposed system, images are first compressed using JPEG and HEIF standards, with different source coding rates applied to ensure similar bandwidth utilization across all multi-qubit systems. The resulting bitstreams are then optionally protected with polar codes. These classical bits are grouped and encoded into multi-qubit quantum states, with encoding sizes ranging from 1 to 8 qubits. Each multi-qubit state undergoes the QFT, transforming it into the quantum frequency domain. This transformation enables the system to exploit spectral sparsity by resiliently transmitting dominant frequency components. This encoded quantum state is transmitted over a noisy quantum channel. At the receiver, the inverse quantum Fourier transform (IQFT) is applied to reconstruct the quantum state in the time domain and map it to the corresponding classical bits. Subsequently, the image bitstream is recovered through optional polar decoding followed by source decoding to reconstruct the images. In addition to channel-coded systems, uncoded systems are also analyzed to understand the intrinsic performance limits of the proposed communication framework. The experimental results demonstrate that the proposed QFT-based multi-qubit communication system outperforms time domain quantum transmission systems and classical communication systems in terms of bit error rate (BER), peak signal-to-noise ratio (PSNR), structural similarity index measure (SSIM), and universal quality index (UQI), providing an error-resilient quantum communication system for next-generation media applications.

The main contributions of this study are as follows:

- The proposal of a novel frequency domain quantum communication framework for compressed image transmission, combining frequency domain processing with quantum superposition to enhance robustness and transmission efficiency.
- Employing multi-qubit quantum state encoding to enable high-dimensional image representations, offering improved resilience to noise compared to single-qubit encoding schemes.
- A demonstration of the superiority of the frequency domain multi-qubit system over its time domain counterpart through comprehensive performance evaluations under varying noise conditions, showing enhanced fidelity and robustness.

The structure of the paper is as follows. Section 2 provides an overview of the related work. Section 3 details the proposed methodology. Section 4 presents the experimental results along with a comprehensive discussion. Finally, Section 5 concludes the paper and outlines potential directions for future research.

## 2. Related Works

Quantum communication represents a transformative shift in how information can be transmitted, leveraging the principles of quantum mechanics [8] to enable faster, efficient, more secure, and fundamentally different modes of communication compared to classical systems. At the heart of this field are two essential quantum phenomena: superposition [9,10] and entanglement [11,12]. Superposition allows a quantum bit to exist

in multiple states simultaneously, unlike classical bits, which are limited to a single binary value at any moment. This characteristic enables more compact and parallel data encoding, offering significant potential to improve communication throughput. Entanglement, on the other hand, is a quantum correlation between particles that links their states regardless of the distance separating them. When two qubits are entangled, measuring the state of one instantly determines the state of the other. This property plays a crucial role in enabling secure communication mechanisms and quantum cryptography [13,14].

In addition, these fundamental principles have been successfully applied to a variety of domains within quantum computing and quantum communication. Entanglement is the foundation of quantum key distribution (QKD) protocols such as BB84 and E91, which provide provably secure encryption keys that cannot be intercepted without detection [15–17]. Similarly, quantum teleportation, another protocol driven by entanglement, allows the transmission of quantum information without physically moving the qubit, laying the foundations for future quantum networks [18,19]. Furthermore, recent advances have shown that quantum techniques can enhance the security of image and video transmission, with several studies exploring how quantum states can be used to securely encrypt and transmit media data over quantum channels [20,21].

Although quantum entanglement has received substantial attention in the field of quantum communication, quantum superposition remains comparatively underexplored, particularly in practical communication systems. A limited number of studies have leveraged superposition primarily for complexity analysis [22–25] or for implementing basic media communication tasks such as image and video transmission using single-qubit encoding schemes [26,27]. However, these approaches do not fully exploit the capacity and parallelism inherent in quantum systems. Additionally, the application of multi-qubit superposition encoding represents a largely unexplored domain in quantum communication, especially for media transmission tasks like image and video transfer. Although single-qubit encoding methods have been applied in basic communication tasks [28,29], the potential of multi-qubit superposition to increase data throughput and robustness has not been fully explored. In contrast, multi-qubit encoding combined with quantum entanglement has been widely employed in other areas of quantum communication, including multi-qubit QKD and quantum teleportation protocols [30–34]. These applications leverage entanglement to ensure secure and high-fidelity information transfer but do not utilize the power of quantum superposition across multiple qubits for data encoding and transmission. This presents a compelling opportunity to extend the use of multi-qubit superposition into the realm of quantum media communication, where its advantages in scalability and efficiency could yield significant improvements. To date, no research has effectively integrated multi-qubit superposition into communication frameworks to enhance performance metrics such as data throughput, noise resilience, and image quality. This gap presents an opportunity to investigate how the unique properties of multi-qubit encoding can revolutionize quantum communication systems, particularly for high-quality, real-time media applications.

While most existing analyses and implementations of quantum communication are grounded in the time domain, the frequency domain presents further untapped potential for advancing system performance, particularly in terms of noise resilience and transmission efficiency. A core tool in this domain is the QFT, which allows quantum data to be transformed from the time domain to the frequency domain [35]. This capability facilitates efficient data representation and compression, making it especially promising for media applications, such as image and video transmission, where both fidelity and bandwidth efficiency are critical.

Traditionally, QFT has been employed primarily in quantum image compression schemes, serving as a mathematical tool to transform image data and reduce qubit requirements. Although several studies have investigated various transforms for data compression and demonstrated their effectiveness [36–40], the QFT has consistently delivered superior compression performance [41]. There are also QKD schemes based on QFT [42] and quantum teleportation protocols [43–45] for secure communication, but these are fundamentally different from the use of QFT as a direct superposition-based encoding technique for image transmission. To the best of our knowledge, no research has yet employed QFT in this direct encoding manner for quantum image communication. Specifically, none of the existing literature has leveraged QFT in combination with multi-qubit quantum superposition encoding to create a unified framework that enables robust transmission in the presence of noise.

Therefore, this research addresses a critical gap in the field of quantum communication by directly integrating QFT into the communication pipeline as a core encoding mechanism. By harnessing the frequency domain processing capabilities of the QFT in conjunction with the inherent advantages of multi-qubit superposition encoding, the proposed system introduces a novel and robust framework for high-fidelity image transmission over quantum networks. This design effectively addresses the limitations of existing state-of-the-art quantum media transmission frameworks, as summarized in Table 1, which provides a comparative overview of related methods.

**Table 1.** Recent advancements in quantum media transmission systems.

Reference	System	Advantages	Limitations
[6]	Single-qubit quantum communication system for image transmission as a classical–quantum hybrid approach	Enhanced noise resilience compared to classical communication systems	High noise sensitivity under severe noise conditions
[28]	Single-qubit quantum communication system with three, five, and seven-qubit quantum error correction codes	Enhanced Noise resilience	Complexity overhead
[29]	Single-qubit quantum MIMO communication system for image transmission	Enhanced noise resilience compared to classical MIMO communication	Noise sensitivity under severe noise conditions
[46]	Single-qubit quantum communication system with three-qubit quantum error correction	Enhanced noise resilience compared to classical communication	Noise sensitivity under severe noise conditions
[47]	Single-qubit quantum MIMO communication system for video transmission	Enhanced noise resilience compared to classical MIMO communication	Noise sensitivity under severe noise conditions
[48]	Secure image transmission	Enhanced security	Only for security purposes

Unlike traditional quantum communication approaches that rely solely on single-qubit encoding or time domain image representation, this research proposes a comprehensive quantum communication architecture that combines the QFT with multi-qubit encoding

(ranging from 1 to 8 qubits) as a scalable and efficient image encoding strategy. This integrated approach not only enhances the utilization of available quantum resources, but also significantly improves the quality of reconstructed images at the receiver. By combining frequency domain transformation with multi-qubit superposition, the proposed system introduces a new paradigm for quantum image transmission, laying the foundation for practical quantum multimedia applications and offering enhanced resilience to noise and channel impairments.

### 3. Methodology

The proposed end-to-end frequency domain multi-qubit quantum image communication system is illustrated in Figure 1. It is designed to be scalable, flexible, and adaptable to multi-qubit quantum encoding schemes, where each logical quantum state can represent between 1 and 8 qubits (Q1-Q8). The upper limit of 8 qubits is purposefully selected to correspond with the 8-bit pixel intensity range (0–255), enabling direct and efficient pixel representation. However, the underlying architecture is not restricted to this limit; it is theoretically extensible to accommodate any qubit encoding size depending on hardware feasibility and application-specific constraints.

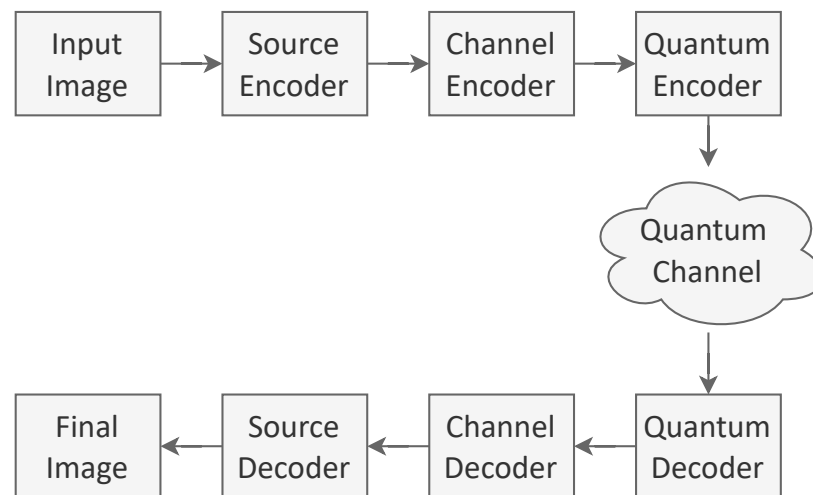


**Figure 1.** The proposed frequency domain multi-qubit quantum communication system.

The system is input-agnostic, capable of processing any type of input image regardless of resolution, content, or structural complexity. For experimental validation, this study employs 50 selected images from the Microsoft COCO dataset [49], a widely recognized benchmark in computer vision. These images exhibit a wide range of spatial information (SI) and encompass diverse natural scenes, object categories, and contextual complexities, providing a representative cross-section of real-world visual data. While the subset comprises 50 images, their deliberate diversity and variability offer sufficient statistical relevance to reflect the challenges encountered in practical scenarios. This selection strikes a balance between computational feasibility and experimental robustness, enabling meaningful performance evaluation under realistic conditions. Moreover, each image undergoes thousands of independent transmission trials across a multidimensional configuration space, including varying channel conditions, qubit encoding sizes (ranging from 1 to 8 qubits), and encoding domains (time and frequency). These extensive trials yield a large volume of data points, enabling statistically meaningful evaluations of both average-case and worst-case performance. Consequently, the aggregated results reflect the system’s robustness and adaptability under diverse and realistic operating conditions.

Once the image is selected, the first step is classical source encoding, where either JPEG or HEIF compression is applied to reduce redundancy while preserving perceptual quality. To ensure equal bandwidth utilization across different multi-qubit systems, we explicitly control the compressed bitstream length for each encoding configuration. The result is a compressed bitstream that represents the image content in binary format. The compressed bitstream then undergoes classical channel encoding using polar codes with a code rate of  $1/2$ . This step introduces structured redundancy, which is crucial for correcting any transmission errors at the receiver. The channel encoded bitstream is then passed to the quantum encoder, which is the core innovation of this system. This module applies multi-qubit encoding by first segmenting the bitstream into bit blocks, where each block represents a multi-qubit state. These blocks, ranging in size from 1 to 8 qubits depending on the system, are then mapped to the frequency domain using the QFT. Each encoded quantum state now represents a transformed version of classical information, distributed across the frequency spectrum of the quantum state space.

These quantum states are then transmitted through a noisy quantum channel. In the simulation environment, we model this quantum channel using generalized quantum noise models, such as bit-flip, phase-flip, depolarizing, amplitude-damping noise, and phase-damping noise. At the receiver, the quantum decoder first identifies the received quantum state in the frequency domain and applies the corresponding IQFT to convert it back into the time domain. Subsequently, quantum measurements on the time domain states produce an estimate of the originally transmitted classical bitstream. This bitstream is then passed through a polar decoder to correct the errors introduced by the noisy channel. Finally, the corrected bitstream is passed through the source decoder (JPEG or HEIF) to reconstruct the image. In addition, the same framework is analyzed without channel coding to evaluate the system's intrinsic performance in the absence of additional error correction.

The following sections provide a detailed explanation of each block in the proposed methodology.

### 3.1. Source Coding

The first stage of the system involves source encoding, which compresses raw image data into a compact binary representation. In this research, we utilize JPEG [50] and HEIF [51] compression algorithms, both of which are widely adopted for image storage and transmission due to their effective balance between compression efficiency and visual quality. Source coding rates are adjusted to align with the same bandwidth across different multi-qubit configurations. To control the compression level during source encoding, we use the quantization parameter (QP) as a tunable variable. In our implementation, lower QP values correspond to higher compression and lower bitrates.

To ensure consistent bandwidth usage across different multi-qubit configurations, Q8 is configured to transmit eight qubits per symbol, while Q1 transmits only a single qubit, resulting in significantly higher quantum bandwidth for Q8. To prevent higher-qubit systems from exceeding the transmission capacity used by lower-qubit systems, we apply stronger compression to higher-qubit configurations.

Consequently, Q8 is assigned a lower QP value, resulting in higher compression and a reduced bitrate. In contrast, Q1 is assigned a higher QP value, allowing lower compression and a higher bitrate. This allocation ensures that all systems produce qubit streams of approximately equal length, maintaining a fair comparison under a unified bandwidth constraint. The same principle is applied to all intermediate qubit levels (Q2 to Q7), such that the product of qubit count and per-symbol bitrate remains roughly constant, i.e.,  $n \times \text{bitrate}_n \approx \text{constant}$ . To meet these targets, QP values are carefully selected. For JPEG compression, QP values of 100, 94, 88, 79, 72, 60, 50, and 40 are used for Q1 to Q8,

respectively. For HEIF compression, the respective QP values are 100, 70, 60, 54, 50, 45, 43, and 41. The output of this stage is a compressed binary bitstream, which significantly reduces the data size while maintaining sufficient image quality for accurate reconstruction after quantum transmission.

### 3.2. Channel Encoding/Decoding

The compressed bitstream is then passed through a classical channel encoder to introduce structured redundancy, which is essential for reliable data recovery in the presence of noise. We employ polar codes [52] with a code rate of  $1/2$ , which means that for every  $k$  bits of data, the encoder produces  $2k$  bits. Polar codes are capacity-achieving for binary input symmetric channels and are particularly well suited for quantum-assisted communication due to their low encoding/decoding complexity, scalability, and provable reliability. Compared to traditional error correction codes such as Reed–Solomon, LDPC, or turbo codes, polar codes offer several distinct advantages, which are as follows:

- Performance in achieving capacity under successive cancellation decoding, which is optimal in the asymptotic regime.
- Lower computational complexity than turbo or LDPC codes, making them more practical for hybrid quantum–classical implementations.
- Recursive and structured construction, which is compatible with efficient quantum circuit implementations.
- Flexible block lengths and code design, allowing adaptation to varying channel conditions and system constraints.

These advantages make polar codes an ideal choice for ensuring robust error correction in quantum transmission scenarios, where quantum noise and decoherence significantly impair the fidelity of transmitted information.

### 3.3. Quantum Encoding

The quantum encoder transforms classical binary data sequences from the time domain into quantum states represented in the frequency domain. This transformation enables efficient quantum representations that are suitable for quantum communication systems. As illustrated in Figure 2, the encoder is structured in sequential layers, as described in the following subsections, with each layer performing a specific mathematical operation.

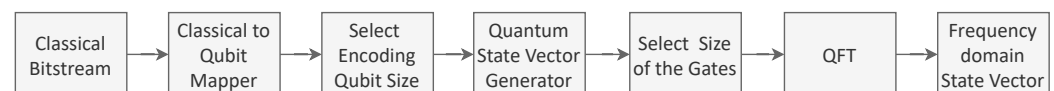


**Figure 2.** The proposed frequency domain multi-qubit quantum encoder.

#### 3.3.1. Mapping a Classical Bit to a Qubit

A classical bit  $b$  is a binary value that can be 0 or 1. To represent this classical bit within a quantum system, we use a qubit, which is a quantum state that resides in a complex two-dimensional vector space known as the Hilbert space  $\mathcal{H}_2$ .

The classical bit  $b$  can be assigned to one of the two quantum computational basis states as follows:

- If  $b = 0$ , it is mapped to the quantum state  $|0\rangle$ ;
- If  $b = 1$ , it is mapped to the quantum state  $|1\rangle$ .

Mathematically, these basis states can be represented by column vectors as in Equations (1) and (2).

$$|0\rangle = \begin{pmatrix} 1 \\ 0 \end{pmatrix} \quad (1)$$

$$|1\rangle = \begin{pmatrix} 0 \\ 1 \end{pmatrix} \quad (2)$$

This classical-to-quantum mapping preserves the classical information in a quantum-compatible format, providing the foundational quantum states required for further processing in quantum communication systems.

### 3.3.2. Qubit Encoding Size Selection and Quantum State Vector Construction

In this process, the system first decides the qubit encoding size ( $n$ ), which can vary from 1 to 8. This parameter defines how many classical bits will be combined and encoded simultaneously into a quantum state. Specifically,  $n = 1$ , and each bit is individually assigned to its respective single qubit computational basis state as in (1) and (2).

Formally, if the input classical bitstream is divided into blocks of length  $n$ , each block can be represented as a bit string ( $b_s$ ) as in Equation (3).

$$\mathbf{b}_s = b_1 b_2 b_3 \dots b_n, \quad b_i \in \{0, 1\} \quad (3)$$

Then, each bit  $b_i$  can be mapped to its corresponding single-qubit state. To form the combined quantum state of the entire block, the individual qubit states are combined using the operation of the tensor product as in Equation (4).

$$|b_1 b_2 \dots b_n\rangle = |b_1\rangle \otimes |b_2\rangle \otimes \dots \otimes |b_n\rangle. \quad (4)$$

For example, when  $n = 2$ , the corresponding bit blocks are 00, 01, 10, and 11. The corresponding two-qubit quantum states are represented in Equations (5)–(8).

$$|00\rangle = |0\rangle \otimes |0\rangle = \begin{pmatrix} 1 \\ 0 \end{pmatrix} \otimes \begin{pmatrix} 1 \\ 0 \end{pmatrix} = \begin{pmatrix} 1 & 0 & 0 & 0 \end{pmatrix}^T \quad (5)$$

$$|01\rangle = |0\rangle \otimes |1\rangle = \begin{pmatrix} 1 \\ 0 \end{pmatrix} \otimes \begin{pmatrix} 0 \\ 1 \end{pmatrix} = \begin{pmatrix} 0 & 1 & 0 & 0 \end{pmatrix}^T \quad (6)$$

$$|10\rangle = |1\rangle \otimes |0\rangle = \begin{pmatrix} 0 \\ 1 \end{pmatrix} \otimes \begin{pmatrix} 1 \\ 0 \end{pmatrix} = \begin{pmatrix} 0 & 0 & 1 & 0 \end{pmatrix}^T \quad (7)$$

$$|11\rangle = |1\rangle \otimes |1\rangle = \begin{pmatrix} 0 \\ 1 \end{pmatrix} \otimes \begin{pmatrix} 0 \\ 1 \end{pmatrix} = \begin{pmatrix} 0 & 0 & 0 & 1 \end{pmatrix}^T \quad (8)$$

Similarly, for any given qubit encoding size  $n$ , multi-qubit quantum state vectors can be systematically constructed from input bit blocks using the tensor product formulation. In general, for an encoding size  $n$ , the resulting quantum state vector resides in a Hilbert space of dimension  $2^n$ . This exponential increase in dimension reflects the power of quantum encoding, allowing compact and efficient representation of multiple classical bits within a single quantum state.

### 3.3.3. Quantum Gate Dimension Selection and Quantum Fourier Transform

To transform a quantum state vector from the time domain into the frequency domain, it is essential to choose a QFT gate whose size matches the dimension of the state vector. The dimension of the quantum state vector depends on the number of qubits ( $n$ ) involved in the encoding and is given by  $2^n \times 1$ . Therefore, the corresponding QFT gate must be a

square matrix of size  $2^n \times 2^n$  to operate correctly in this state. For example, if the quantum state vector has a length of  $4 \times 1$  (which corresponds to  $n = 2$  qubits), then the QFT gate must be a  $4 \times 4$  matrix. For 3 qubits ( $n = 3$ ), the state vector length is 8, and thus the gate size must be  $8 \times 8$ . This scaling principle holds true for any number of qubits.

In addition, the QFT for a system of  $n$  qubits, where the dimension is  $N = 2^n$ , can be represented by the unitary matrix  $F_N$ . When applied to a computational basis state  $|x\rangle$ , the QFT transforms it into a frequency domain superposition state given by Equation (9).

$$F_N |x\rangle = \frac{1}{\sqrt{N}} \sum_{k=0}^{N-1} e^{2\pi i \frac{xk}{N}} |k\rangle \tag{9}$$

This transformation expresses the input  $|x\rangle$  as a linear combination of all basis states  $|k\rangle$ , where each term includes a complex phase factor  $e^{2\pi i \frac{xk}{N}}$  encoding frequency information. The factor  $\frac{1}{\sqrt{N}}$  normalizes the state, ensuring that the overall transformation is unitary and preserves the quantum state norm.

Furthermore, the QFT matrix  $F_N$ , where  $N = 2^n$ , can be constructed as shown in Equation (10).

$$F_N = \frac{1}{\sqrt{N}} \begin{pmatrix} 1 & 1 & 1 & \dots & 1 \\ 1 & \omega & \omega^2 & \dots & \omega^{N-1} \\ 1 & \omega^2 & \omega^4 & \dots & \omega^{2(N-1)} \\ \vdots & \vdots & \vdots & \ddots & \vdots \\ 1 & \omega^{N-1} & \omega^{2(N-1)} & \dots & \omega^{(N-1)^2} \end{pmatrix} \tag{10}$$

where  $\omega$  is the primitive  $N^{\text{th}}$  root of unity, as defined in Equation (11).

$$\omega = e^{\frac{2\pi i}{N}} \tag{11}$$

For example, with an encoding size of  $n = 2$ , the QFT matrix  $F_4$  is given by the  $4 \times 4$  matrix in Equation (12).

$$F_4 = \frac{1}{2} \begin{pmatrix} 1 & 1 & 1 & 1 \\ 1 & i & -1 & -i \\ 1 & -1 & 1 & -1 \\ 1 & -i & -1 & i \end{pmatrix} \tag{12}$$

This definition scales naturally to any number of qubits  $n$ , where each entry of  $F_N$  is computed using the matrix defined in Equation (10). The QFT matrix acts on the quantum state vector, converting it from its original time-based representation into the frequency domain by multiplying the state vector by  $F_N$ . For an example, consider the four basis vectors representing two-qubit states:  $|00\rangle$ ,  $|01\rangle$ ,  $|10\rangle$ , and  $|11\rangle$ . Applying the  $F_4$  transform to each input yields distinct vectors in the frequency domain, as shown in Equations (13) through (16).

$$F_4 |00\rangle = \frac{1}{2} \begin{pmatrix} 1 & 1 & 1 & 1 \end{pmatrix}^T = \frac{1}{2} (|00\rangle + |01\rangle + |10\rangle + |11\rangle) \tag{13}$$

$$F_4 |01\rangle = \frac{1}{2} \begin{pmatrix} 1 & i & -1 & -i \end{pmatrix}^T = \frac{1}{2} (|00\rangle + i|01\rangle - |10\rangle - i|11\rangle) \tag{14}$$

$$F_4 |10\rangle = \frac{1}{2} \begin{pmatrix} 1 & -1 & 1 & -1 \end{pmatrix}^T = \frac{1}{2} (|00\rangle - |01\rangle + |10\rangle - |11\rangle) \tag{15}$$

$$F_4 |11\rangle = \frac{1}{2} \begin{pmatrix} 1 & -i & -1 & i \end{pmatrix}^T = \frac{1}{2} (|00\rangle - i|01\rangle - |10\rangle + i|11\rangle) \tag{16}$$

These results demonstrate how each two-qubit basis state in the time domain is uniquely transformed into a complex-valued vector in the frequency domain via the QFT. This unitary QFT matrix acts as a bridge, enabling the representation of quantum information in the frequency domain, which is particularly useful for subsequent quantum processing and communication steps. In addition, these transformed vectors demonstrate how each original qubit basis state corresponds to a distinct vector in the frequency domain, each representing a column of the QFT matrix. This transformation is fundamental to quantum algorithms and communication techniques that exploit frequency domain representations.

### 3.4. Quantum Channel

Within our simulation framework, quantum states transmitted in the frequency domain are exposed to a range of quantum noise processes to emulate realistic communication environments [53]. The modeled noise channel include bit-flip, phase-flip, depolarizing, amplitude damping, and phase damping noises.

The bit-flip noise, characterized by an error probability  $\alpha$ , randomly inverts the state of a qubit between  $|0\rangle$  and  $|1\rangle$ . The corresponding quantum operation on a density matrix  $\rho$  is expressed as Equation (17). Here,  $X$  denotes the Pauli-X operator.

$$\mathcal{N}_{\text{bf}}(\rho) = \alpha X\rho X^\dagger + (1 - \alpha)\rho \tag{17}$$

Similarly, phase-flip noise introduces phase errors with a probability  $\beta$ , altering the sign of the  $|1\rangle$  component in the superposition. The operation is given by Equation (18). Here,  $Z$  denotes the Pauli-Z operator.

$$\mathcal{N}_{\text{pf}}(\rho) = \beta Z\rho Z^\dagger + (1 - \beta)\rho \tag{18}$$

For depolarizing noise, the state  $\rho$  is partially replaced by the maximally mixed state with a probability  $\gamma$ , modeling complete uncertainty in the state. The map is represented as Equation (19). Here,  $X$ ,  $Y$ , and  $Z$  denote the Pauli-X, Y, and Z operators.

$$\mathcal{N}_{\text{dp}}(\rho) = (1 - \gamma)\rho + \frac{\gamma}{3}(X\rho X^\dagger + Y\rho Y^\dagger + Z\rho Z^\dagger) \tag{19}$$

The noise of amplitude damping, characterized by a damping probability  $\delta$ , models the loss of quantum energy, such as spontaneous emission, using the formalism shown in Equation (20), and is represented by Kraus operators as given in Equation (21).

$$\mathcal{N}_{\text{ad}}(\rho) = E_0\rho E_0^\dagger + E_1\rho E_1^\dagger \tag{20}$$

$$E_0 = \begin{pmatrix} 1 & 0 \\ 0 & \sqrt{1-\delta} \end{pmatrix}, \quad E_1 = \begin{pmatrix} 0 & \sqrt{\delta} \\ 0 & 0 \end{pmatrix} \tag{21}$$

In contrast, phase damping, modeled with probability  $\theta$ , causes dephasing without altering the populations of basis states. The transformation is described using Equation (22).

$$\mathcal{N}_{\text{pd}}(\rho) = F_0\rho F_0^\dagger + F_1\rho F_1^\dagger$$

$$\text{where } F_0 = \begin{pmatrix} 1 & 0 \\ 0 & \sqrt{1-\theta} \end{pmatrix}, \quad F_1 = \begin{pmatrix} 0 & 0 \\ 0 & \sqrt{\theta} \end{pmatrix} \tag{22}$$

To model the aggregate effect of these types of noise on a qubit, we combine individual noises with their respective probabilities, as shown in Equation (23).

$$\mathcal{N}_{\text{total}}(\rho) = \alpha \mathcal{N}_{\text{bf}}(\rho) + \beta \mathcal{N}_{\text{pf}}(\rho) + \gamma \mathcal{N}_{\text{dp}}(\rho) + \delta \mathcal{N}_{\text{ad}}(\rho) + \theta \mathcal{N}_{\text{pd}}(\rho) \quad (23)$$

Here,  $\rho$  represents the quantum frequency state subject to environmental noise. The dagger symbol  $\dagger$  denotes the Hermitian conjugate (complex conjugate transpose). By varying the probabilities of noise in relation to the signal-to-noise ratio (SNR) [54], we evaluate the robustness of the system to different types of decoherence and disturbances within the quantum channel. To control the SNR during simulation, we normalize the signal power and vary the noise power across different conditions. The SNR in decibels is defined as in Equation (24).

$$\text{SNR (dB)} = 10 \log_{10} \left( \frac{P_{\text{signal}}}{P_{\text{noise}}} \right) \quad (24)$$

where  $P_{\text{signal}}$  is fixed and  $P_{\text{noise}}$  is adjusted accordingly.

Based on this, the total quantum noise probability is defined as an inverse function of the linear SNR, as shown in Equation (25), ensuring that higher SNR values correspond to lower overall noise levels (25).

$$p_{\text{total}} = \min \left( 1, \frac{1}{1 + 10^{\text{SNR}/10}} \right) \quad (25)$$

This total noise probability is then distributed among five types of quantum noise: bit-flip ( $\alpha$ ), phase-flip ( $\beta$ ), depolarizing ( $\gamma$ ), amplitude damping ( $\delta$ ), and phase damping ( $\theta$ ). To assign these probabilities dynamically and non-deterministically, five independent random values are generated, as shown in Equation (26), which act as weighting coefficients.

$$r_1, r_2, r_3, r_4, r_5 \sim \mathcal{U}(0, 1) \quad (26)$$

These values are normalized and scaled to ensure that each noise type receives a proportion of the total noise, as shown in Equation (27).

$$[\alpha, \beta, \gamma, \delta, \theta] = \left( \frac{r_i}{\sum_{j=1}^5 r_j} \right) \cdot p_{\text{total}} \quad (27)$$

This assignment satisfies the total noise constraint, as defined in Equation (28).

$$\alpha + \beta + \gamma + \delta + \theta = p_{\text{total}} \quad (28)$$

This approach allows the overall noise level to be governed by the SNR, while the contribution from each individual noise type varies across simulation runs. This models practical quantum communication environments, where noise is both signal-dependent and heterogeneous in nature.

### 3.5. Quantum Decoding

The quantum decoder serves to reverse the quantum encoding process by transforming the received frequency domain quantum state into its original time domain representation. As shown in Figure 3, the entire frequency domain quantum state vector is processed directly by the quantum decoder. The first step in the decoding process is to determine the dimensionality of the received quantum state in order to select the appropriate IQFT gate size. This is performed by measuring the dimension of the received quantum state. The IQFT is then applied to transform the state from the frequency basis to the time domain. Finally, the qubit generator performs quantum measurements by checking the received

quantum states, mapping them to the corresponding qubits, and yielding a classical binary stream corresponding to the transmitted data.

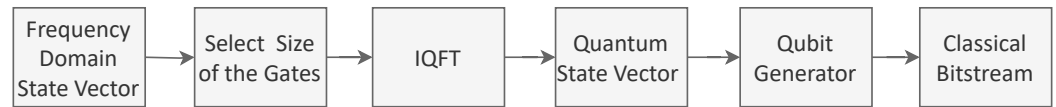


**Figure 3.** The proposed frequency domain quantum decoder.

### 3.5.1. Mathematical Process of Quantum Decoding in Noiseless Situation

Mathematically, the IQFT is the conjugate transpose of the QFT operator, defined as in Equation (29).

$$F_{IQFT} = F_{QFT}^\dagger \tag{29}$$

Let the received frequency domain state be represented as  $|\Psi_f\rangle \in \mathbb{C}^{2^n}$ , where  $n$  is the number of qubits involved in the quantum representation, and  $\mathbb{C}^{2^n}$  denotes the complex Hilbert space of dimension  $2^n$  that describes all possible superpositions of the  $n$ -qubit system. The decoder applies the IQFT transformation as in Equation (30) to convert the quantum state from the frequency domain to the time domain.

$$|\Psi_t\rangle = F_{IQFT} |\Psi_f\rangle \tag{30}$$

Here,  $|\Psi_t\rangle$  is the reconstructed quantum state in the time domain. The final measurement step projects  $|\Psi_t\rangle$  onto the computational basis, producing a classical bitstring.

### 3.5.2. Mathematical Process of Quantum Decoding in Noisy Situation

Due to the presence of channel noise, the received state may deviate from the ideal QFT basis vectors. Let  $|\Phi_f\rangle$  be the noisy received vector as represented in Equation (31).

$$|\Phi_f\rangle = |\Psi_f\rangle + |v\rangle \tag{31}$$

where  $|v\rangle$  is a complex-valued noise vector with  $\| |v\rangle \| \ll 1$ . To identify the original transmitted frequency state, we perform a nearest-vector match in the frequency domain. Suppose the set of ideal QFT basis states is  $\mathcal{B} = \{|\phi_j\rangle\}_{j=0}^{2^n-1}$ . The decoder estimates the symbol index  $j'$  according to the Equation (32).

$$j' = \arg \min_j \| |\Phi_f\rangle - |\phi_j\rangle \| \tag{32}$$

Once the best match  $|\phi_{j'}\rangle$  is determined, it is assumed that it is the transmitted basis state. The IQFT transform is then applied as in Equation (33).

$$|\tilde{\Psi}_t\rangle = F_{IQFT} |\phi_{j'}\rangle \tag{33}$$

Measurement of  $|\tilde{\Psi}_t\rangle$  yields the estimated classical bitstream  $\hat{\mathbf{b}} \in \{0, 1\}$ .

In summary, the full quantum state is preserved throughout transmission, and recovery is based on comprehensive vector matching. Unlike schemes that rely on inspecting individual elements (such as a particular amplitude or phase), this approach enhances robustness by utilizing the global structure of the quantum state in the frequency domain.

### 3.6. Hardware Implementation of Quantum Fourier Transform

The QFT is realized in hardware through a sequence of quantum gates that manipulate qubits to perform the discrete Fourier transform in the quantum domain. The primary building blocks in this hardware implementation are the Hadamard gates and controlled

phase-rotation gates. The Hadamard gate acts on a single qubit and creates an equal superposition of computational basis states. Its matrix representation is shown in Equation (34).

$$H = \frac{1}{\sqrt{2}} \begin{bmatrix} 1 & 1 \\ 1 & -1 \end{bmatrix} \tag{34}$$

This gate transforms a qubit state  $|0\rangle$  into  $\frac{1}{\sqrt{2}}(|0\rangle + |1\rangle)$  and  $|1\rangle$  into  $\frac{1}{\sqrt{2}}(|0\rangle - |1\rangle)$ , thereby enabling the superposition necessary for parallel phase encoding.

To encode phase relationships between qubits, the QFT circuit employs controlled phase-rotation gates. The general phase gate applied conditionally is given by Equation (35).

$$P(\theta) = \begin{bmatrix} 1 & 0 \\ 0 & e^{i\theta} \end{bmatrix} \tag{35}$$

where the rotation angle  $\theta$  depends on the relative position between the control and target qubits. Specifically, for the controlled- $R_k$  gate, the phase angle is  $\theta = \frac{2\pi}{2^k}$ , with  $k$  indicating the distance between qubits.

For the three-qubit QFT circuit example as shown in Figure 4, the rotation matrices for  $R_2$  and  $R_3$  are shown in Equations (36) and (37).

$$R_2 = \begin{bmatrix} 1 & 0 \\ 0 & e^{2\pi i/4} \end{bmatrix} \tag{36}$$

$$R_3 = \begin{bmatrix} 1 & 0 \\ 0 & e^{2\pi i/8} \end{bmatrix} \tag{37}$$

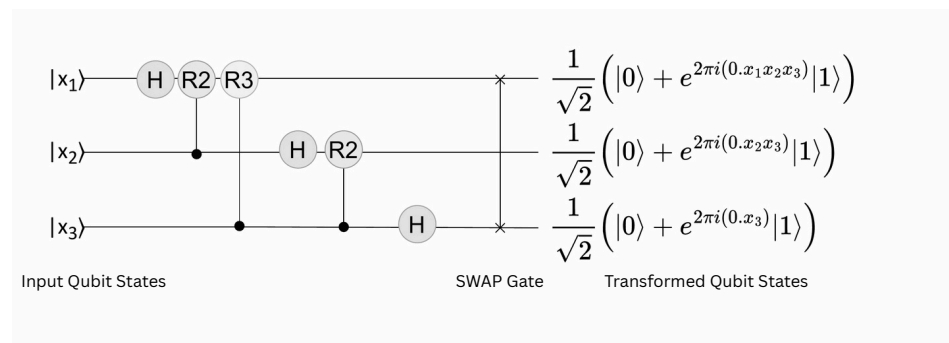


**Figure 4.** The implementation of the three-qubit QFT circuit.

In the three-qubit QFT circuit as shown in Figure 4, the procedure begins by applying a Hadamard gate to the most significant qubit  $x_1$ . This operation generates a superposition, setting the stage for subsequent phase rotations. Following this, controlled phase rotations  $R_2$  and  $R_3$  are applied, controlled by  $x_1$  and targeting  $x_2$  and  $x_3$  respectively, introducing precise phase shifts conditioned on the qubit states. Next, the second qubit  $x_2$  undergoes a Hadamard transformation to form its own superposition, followed by a controlled- $R_2$  gate between  $x_2$  and  $x_3$ . The least significant qubit  $x_3$  only experiences a Hadamard gate, as no qubits lie beyond it for further conditional phase encoding. Due to the construction of the QFT circuit, the final qubit order is reversed relative to the input. To correct this ordering in hardware, the SWAP gates [55] are applied, exchanging the qubit positions to restore the original logical sequence. The output state of the QFT circuit can be expressed as a tensor product of superposition and phase-encoded qubits as shown in Equation (38).

$$\text{QFT}(|x_1x_2x_3\rangle) = \frac{1}{\sqrt{8}} \left( |0\rangle + e^{2\pi i \cdot 0 \cdot x_3} |1\rangle \right) \otimes \left( |0\rangle + e^{2\pi i \cdot 0 \cdot x_2 x_3} |1\rangle \right) \otimes \left( |0\rangle + e^{2\pi i \cdot 0 \cdot x_1 x_2 x_3} |1\rangle \right) \tag{38}$$

Here, each qubit accumulates phase information corresponding to the binary fractional values formed by itself and the less significant qubits, confirming both the accuracy of the QFT operation and its underlying theoretical principles. Similarly, by reversing these quantum gates, we can construct the IQFT hardware implementation [56].

### 3.7. Time Domain Multi-Qubit System

To compare the performance of the proposed frequency domain multi-qubit system, a time domain quantum communication system is proposed under the same bandwidth, channel coding, and source coding rates. This subsection presents a detailed description of the benchmarked time domain multi-qubit system.

In the time domain version of the proposed multi-qubit framework, the transformation from classical to quantum states does not utilize the QFT matrix as in the frequency domain scenario. Instead, the Hadamard transform is employed to generate superposition states. The fundamental building block is the single-qubit Hadamard gate, defined in Equation (34), which transforms a basis state into an equal superposition of basis states. To extend this operation to higher-dimensional quantum systems with  $n$  qubits, we construct the Hadamard operator using the tensor product of  $n$  single-qubit Hadamard matrices. This operation creates a  $2^n \times 2^n$  transformation matrix, ensuring that the resulting quantum system exists in a superposition across all  $2^n$  basis states.

For example, in a two-qubit system ( $n = 2$ ), the composite Hadamard transformation is given by the tensor product, as shown in Equation (39).

$$H \otimes H = \left( \frac{1}{\sqrt{2}} \begin{pmatrix} 1 & 1 \\ 1 & -1 \end{pmatrix} \right) \otimes \left( \frac{1}{\sqrt{2}} \begin{pmatrix} 1 & 1 \\ 1 & -1 \end{pmatrix} \right) = \frac{1}{2} \begin{pmatrix} 1 & 1 & 1 & 1 \\ 1 & -1 & 1 & -1 \\ 1 & 1 & -1 & -1 \\ 1 & -1 & -1 & 1 \end{pmatrix} \tag{39}$$

Applying this matrix to computational basis states generates distinct superposition states. For example, encoding the basis state  $|00\rangle$  corresponds to applying the Hadamard transformation to the vector  $[1 \ 0 \ 0 \ 0]^T$ , resulting in the superposition state shown in Equation (40).

$$H^{\otimes 2} \begin{pmatrix} 1 & 0 & 0 & 0 \end{pmatrix}^T = \frac{1}{2} \begin{pmatrix} 1 & 1 & 1 & 1 \end{pmatrix}^T \tag{40}$$

Similarly, encoding the basis states  $|01\rangle$ ,  $|10\rangle$ , and  $|11\rangle$  yields the results shown in Equations (41)–(43).

$$H^{\otimes 2} \begin{pmatrix} 0 & 1 & 0 & 0 \end{pmatrix}^T = \frac{1}{2} \begin{pmatrix} 1 & -1 & 1 & -1 \end{pmatrix}^T \tag{41}$$

$$H^{\otimes 2} \begin{pmatrix} 0 & 0 & 1 & 0 \end{pmatrix}^T = \frac{1}{2} \begin{pmatrix} 1 & 1 & -1 & -1 \end{pmatrix}^T \tag{42}$$

$$H^{\otimes 2} \begin{pmatrix} 0 & 0 & 0 & 1 \end{pmatrix}^T = \frac{1}{2} \begin{pmatrix} 1 & -1 & -1 & 1 \end{pmatrix}^T \tag{43}$$

These superposition vectors are then transmitted through a quantum channel, which may introduce various types of noise as detailed in Section 3.4. At the receiver, quantum decoding is performed by reapplying the same Hadamard transformation since the Hadamard matrix is self-inverse, as shown in Equation (44).

$$H = H^{-1} \quad (44)$$

For example, applying the Hadamard matrix again to the received (noiseless) superposition state from Equation (43) restores the original basis state according to Equation (45).

$$H^{\otimes 2} \left( \frac{1}{2} \begin{pmatrix} 1 & -1 & -1 & 1 \end{pmatrix} \right)^T = \begin{pmatrix} 0 & 0 & 0 & 1 \end{pmatrix}^T \quad (45)$$

In the presence of noise, this process still allows the received superposition state to match to the nearest predefined superposition state by using the Euclidean distance. Then, the inverse Hadamard transformation is applied to that state, recovering the quantum states. From the retrieved quantum state vector, the transmitted classical bit pattern can be effectively recovered through measurement.

Finally, the classical bitstreams received from time domain multi-qubit systems are processed through channel decoding, followed by source decoding, to reconstruct the original images. Simulations are performed entirely within a mathematical framework implemented in Python 3, providing theoretical validation of the performance and robustness of the proposed system under various noise conditions.

## 4. Results and Discussion

This section presents the performance evaluation of the proposed framework using BER, PSNR, SSIM, and UQI as key performance metrics. Results are reported for both frequency domain and time domain multi-qubit systems. A comparative analysis between these two domains is conducted to highlight their respective strengths and weaknesses. To ensure statistical reliability, the evaluation is conducted on a dataset of 50 images, with 1000 trials per image. The reported results represent the average performance across all test cases. The framework is tested using JPEG and HEIF image formats in channel-coded and uncoded transmission scenarios, allowing a thorough examination of its performance under varied source coding and channel conditions. The results validate the robustness and efficiency of the proposed system across different communication environments.

The following subsections provide a detailed presentation and analysis of the results for each communication system.

### 4.1. Frequency Domain Multi-Qubit Framework for JPEG Image Transmission

Performance analysis of the uncoded frequency domain multi-qubit system for JPEG image transmission is carried out by measuring image quality metrics under varying channel SNR levels, as illustrated in Figure 5a–d. The analysis highlights the impact of different qubit encoding sizes (from Q1 to Q8) on transmission quality and robustness.

The BER performance across different qubit encoding sizes (Q1 to Q8), as shown in Figure 5a, reveals a clear trend: as the qubit encoding size increases, the BER consistently decreases for a given channel SNR. This behavior reflects enhanced transmission reliability, as larger qubit states provide greater resilience to channel noise. Specifically, Q8 encoding demonstrates the lowest BER across all evaluated SNR levels, indicating a significant reduction in transmission errors and more effective preservation of the underlying bitstream. As shown in Figure 5b, the PSNR improves with increasing channel SNR and higher qubit encoding sizes. At each SNR level, systems employing larger qubit sizes achieve higher PSNR values, reflecting reduced distortion and noise in the reconstructed image. This enhancement is attributed to the increased representational capacity of higher-dimensional Hilbert spaces and the effective use of superposition and phase encoding in the frequency domain. The Q8 configuration consistently delivers the highest image quality, with greater sharpness and detail fidelity. In contrast, the Q1 system shows the lowest PSNR, particu-

larly under low SNR conditions, where its limited encoding capacity results in perceptible image degradation.

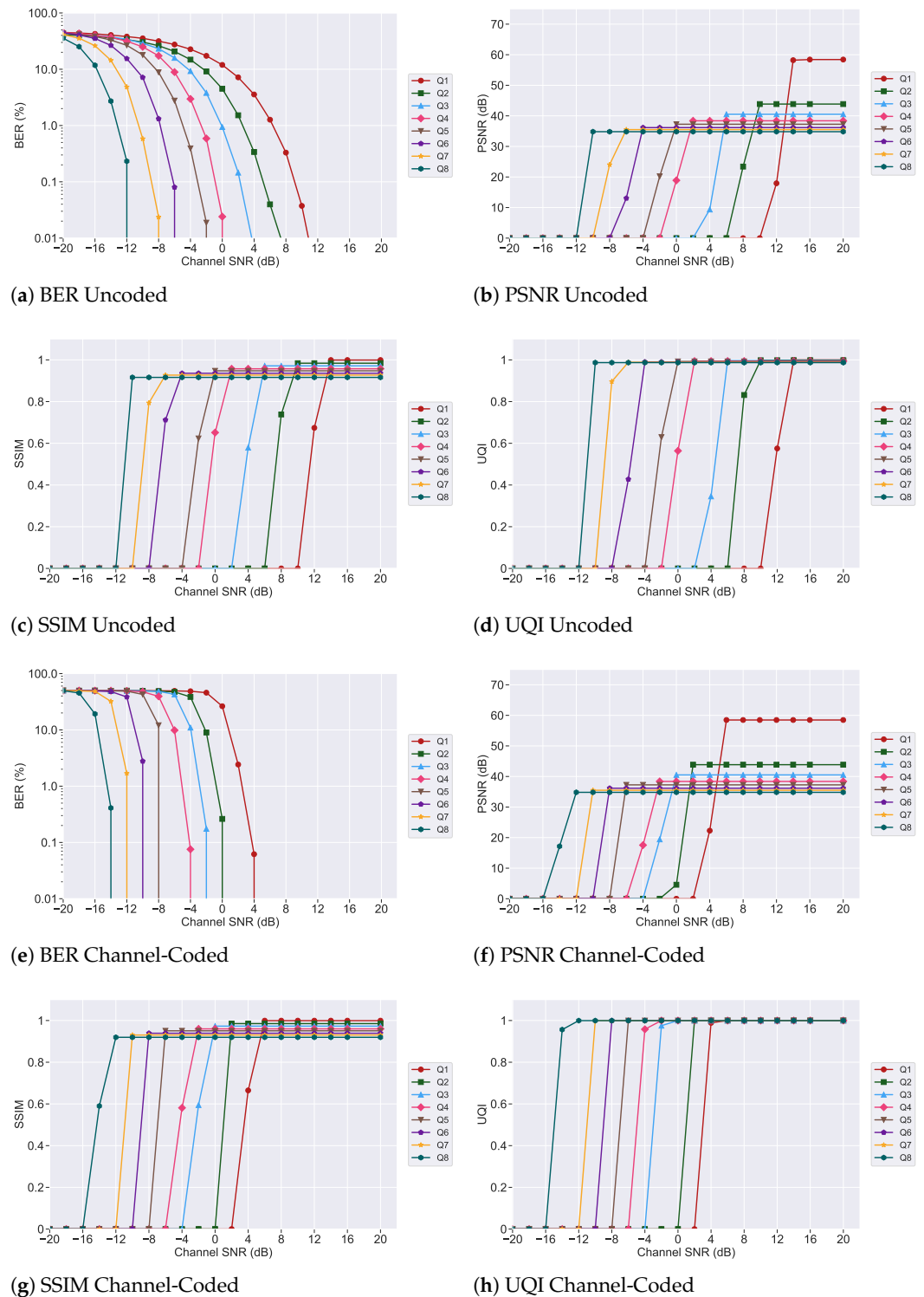


**Figure 5.** Performance evaluation of BER, PSNR, SSIM, and UQI for JPEG images transmitted using frequency domain encoding across varying SNR levels, under both uncoded and channel-coded conditions.

The SSIM results, shown in Figure 5c, quantify the perceptual similarity between the original and received images, with higher SSIM values (closer to 1) indicating better structural preservation. The results demonstrate that SSIM improves with increasing channel

SNR and larger qubit encoding sizes. In particular, Q8 consistently maintains superior structural integrity, even under lower SNR conditions, highlighting the effectiveness of higher-dimensional qubit encodings in preserving image perceptual quality. Similarly, the UQI results in Figure 5d reinforce these observations. UQI values approach 1 with increasing SNR, and higher qubit encoding sizes achieve a given UQI value at significantly lower SNR levels. For example, the Q8 configuration attains near-perfect UQI performance under much noisier conditions compared to Q1, demonstrating the superior efficiency and robustness of higher-dimensional qubit encodings in preserving image fidelity.

Overall, the uncoded JPEG frequency domain multi-qubit system demonstrates a consistent improvement in image transmission quality as the qubit encoding size increases from Q1 to Q8. These improvements across BER, PSNR, SSIM, and UQI metrics are primarily due to the expanded information-carrying capacity of larger qubit encodings and their enhanced resilience to noise through the exploitation of quantum superposition and frequency domain phase encoding. Although larger qubit sizes require more physical resources and quantum operations, their superior performance makes them highly suitable for applications where image fidelity is critical.

The performance of the frequency domain multi-qubit system for JPEG image transmission under channel-coded conditions is evaluated using the same set of image quality metrics as in the uncoded scenario. The results, shown in Figure 5e–h, provide more detailed insight into how classical channel coding improves the general resilience and fidelity of quantum-based image transmission, particularly when used with varying qubit encoding sizes. As illustrated in Figure 5e, the application of channel coding leads to a significant improvement in BER performance in all qubit configurations, as expected. Compared to the uncoded baseline, the BER values decrease significantly, even at modest SNR levels. This sharp reduction in BER with increasing channel SNR reflects the effectiveness of the channel code in mitigating the impact of noise and correcting transmission errors. Importantly, the beneficial trend observed in the uncoded scenario, where larger qubit sizes correspond to lower BER, remains consistent in the coded scenario. This indicates that higher-dimensional qubit encodings, when combined with robust channel coding techniques, produce synergistic gains in transmission reliability. For example, the Q8 configuration consistently achieves near-zero BER at much lower SNR values than Q1, underscoring the advantage of leveraging both quantum-level encoding scalability and classical error correction.

The PSNR results, depicted in Figure 5f, further support this observation by quantifying the fidelity of the image reconstruction. As SNR increases, PSNR values show a marked improvement in the presence of channel coding compared to the uncoded scenario. Notably, the improvement is more pronounced for higher qubit configurations. The Q8 encoding not only achieves the highest PSNR but does so at significantly lower SNR thresholds, indicating that the combination of strong quantum encoding and effective classical error correction contributes to superior reconstruction quality in terms of signal fidelity. The SSIM results, presented in Figure 5g, further validate the improvements in perceptual image quality of the reconstructed images. With channel coding, SSIM values approach unity more rapidly as the channel SNR increases, compared to the uncoded scenario. This indicates a more effective preservation of structural content in the transmitted images. Moreover, SSIM consistently improves with larger qubit encoding sizes, highlighting the enhanced capability of the system to maintain perceptual fidelity under noise. Finally, the UQI results, as shown in Figure 5h, demonstrate the system's ability to maintain high visual quality. UQI values converge to 1 with significantly lower SNRs than in the uncoded scenario, reflecting the robust impact of error correction, as expected. Among all

configurations, the Q8 system again achieves the best performance, exhibiting high-quality reconstruction even under adverse channel conditions.

Based on the results, the application of classical channel coding yields significant improvements in all key metrics, including BER, PSNR, SSIM, and UQI. It effectively reduces transmission errors, enhances signal reconstruction, and greatly improves perceptual image quality. Furthermore, increasing the size of the qubit encoding from Q1 to Q8 consistently strengthens these benefits by harnessing the enhanced representational capacity and robustness of the quantum system. Therefore, the combination of channel coding with higher-dimensional frequency domain quantum encoding proves to be a highly effective strategy for reliable and high-quality image transmission in noisy quantum communication environments.

#### 4.2. Time Domain Multi-Qubit Framework for JPEG Image Transmission

Following the frequency domain analysis, we evaluate the performance of the time domain multi-qubit image transmission system for JPEG image transmission under comparable experimental conditions. This comparative study covers both uncoded and channel-coded scenarios, highlighting how high-dimensional time domain encoding influences the system's robustness and image quality in the time domain. In the uncoded time domain scenario, performance trends closely mirror those observed in the frequency domain, although with comparatively reduced gains across all metrics. As illustrated in Figure 6a–d, increasing the channel SNR results in a steady reduction in BER across all qubit encoding sizes, with Q8 once again outperforming the lower-dimensional encodings. However, the rate of BER improvement is generally slower than in the frequency domain scenario, reflecting the increased susceptibility of time domain encodings to channel noise. Figure 6a–d further confirm that although BER, PSNR, SSIM, and UQI improve with larger qubit sizes and higher SNR, their values at the corresponding channel SNR levels remain lower compared to those observed in the frequency domain system. These findings suggest that time domain representations are more sensitive to quantum noise, which affects the integrity of the received image.

In contrast, the channel-coded time domain scenario demonstrates a notable improvement in all performance metrics compared to the uncoded scenario, reinforcing the pivotal role of error correction in quantum communication. As shown in Figure 6e–h, the use of polar code-based channel coding significantly accelerates the reduction of BER with increasing SNR compared to the uncoded case. However, overall improvements remain limited compared to the channel-coded frequency domain scenario. This difference is attributed to the relatively lower noise resilience of time domain quantum encoding, even with the application of channel coding.

#### 4.3. Comparing Transmission Efficiency Between Time Domain and Frequency Domain Systems for JPEG Image Transmission

A comparative study between time domain (TQ1–TQ8) and frequency domain (FQ1–FQ8) multi-qubit systems reveals notable differences in performance behavior and computational complexity across varying qubit sizes. In the uncoded scenario, where no classical error correction is employed, the frequency domain encoding achieves significantly lower BER and higher values of PSNR, SSIM, and UQI compared to the time domain system. These results, summarized in Figure 7a–d, clearly demonstrate that the frequency domain system consistently outperforms the time domain approach in all performance metrics. This highlights the superior noise resilience of the frequency domain system and its ability to preserve both structural and perceptual image quality. In contrast, the time domain system, which relies solely on amplitude-based superposition in the high-dimensional Hilbert

space, experiences more rapid performance degradation under noisy conditions because of the absence of phase encoding diversity present in the frequency domain approach.

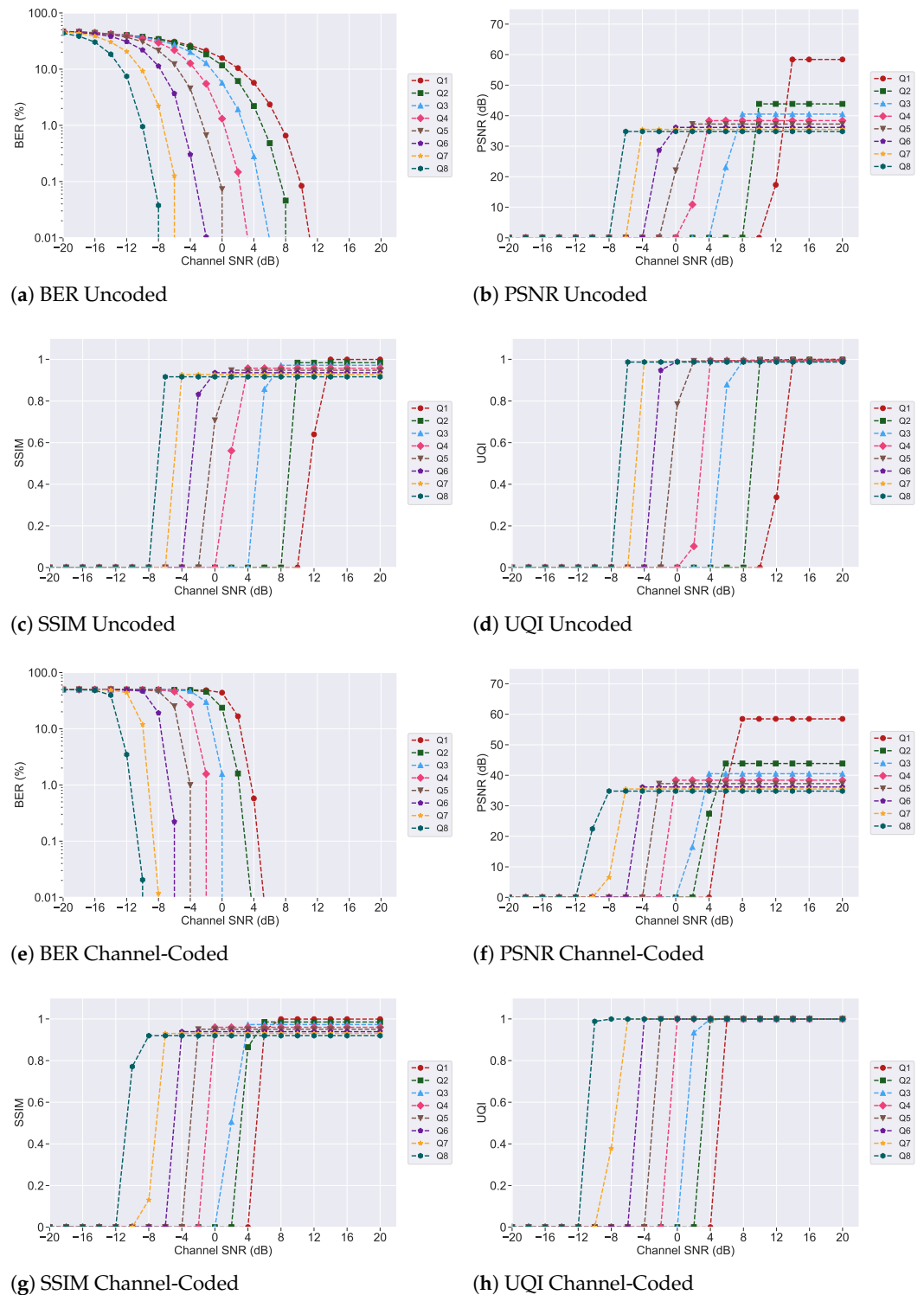


**Figure 6.** Performance evaluation of BER, PSNR, SSIM, and UQI for JPEG images transmitted using time domain encoding across varying SNR levels, under both uncoded and channel-coded conditions.

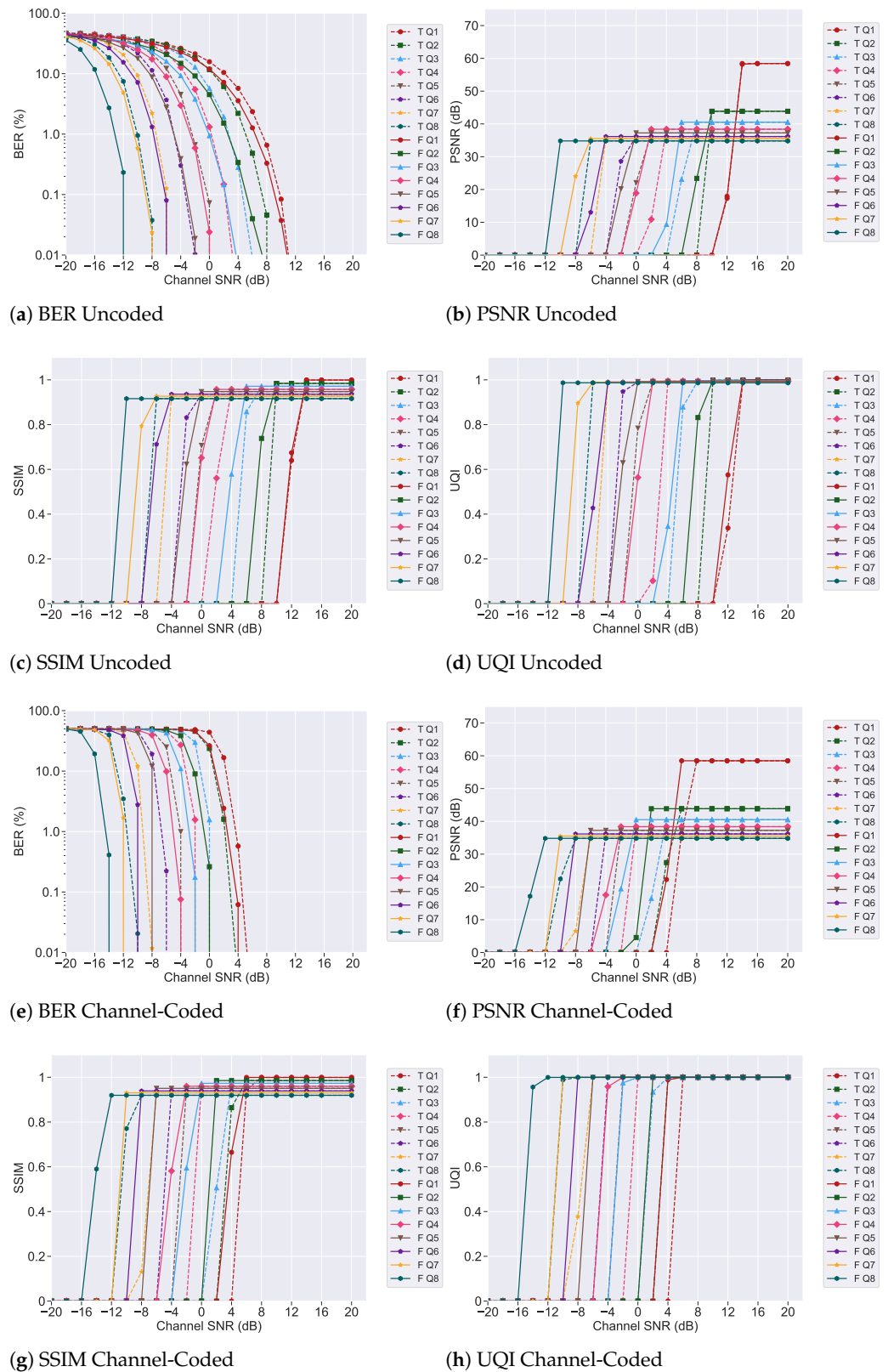


**Figure 7.** Comparative analysis of BER, PSNR, SSIM, and UQI for JPEG image transmission using time domain and frequency domain encoding schemes over varying SNR levels, under both uncoded and channel-coded conditions.

When channel coding is introduced through the use of polar codes, both systems (Figure 7e–h) exhibit improved performance; however, the frequency domain system main-

tains a clear advantage. This persistent superiority stems from the integration of QFT in the frequency domain approach, which combines high-dimensional superposition and phase encoding. This dual encoding mechanism enables the system to exploit both the amplitude and phase degrees of freedom, allowing more efficient state representation, enhanced distinguishability between quantum states, and increased robustness to noise perturbations. The time domain system, on the other hand, remains constrained to amplitude-based superposition and lacks this additional layer of phase diversity, thereby limiting its overall performance. In addition, the performance gap between time domain and frequency domain encoding is relatively small in single-qubit systems because the benefits of the QFT are limited at such low dimensionality. With only one qubit, there is no opportunity to exploit phase relationships or interference effects across multiple qubits, which are the key advantages of frequency domain processing as described in Section 3.6. As the number of qubits increases, frequency domain encoding becomes more effective, leveraging complex state interactions and phase encoding to significantly improve robustness and image quality.

#### 4.4. Frequency Domain Multi-Qubit Framework for Heif Image Transmission

This section evaluates the performance of the frequency domain multi-qubit image transmission system using HEIF-compressed images, focusing first on the uncoded configuration (Figure 8a–d). The results demonstrate a strong consistency with the JPEG-based analysis presented in Section 4.1, highlighting the adaptability of the framework across different image source coding formats. Across all four performance metrics, similar trends are observed, reinforcing the generalizability and robustness of the proposed system. Specifically, even in the absence of classical channel coding, the system exhibits improved noise resilience and image fidelity as the qubit encoding size increases. At lower SNRs, BER increases as expected; however, higher qubit configurations (particularly Q6 to Q8) significantly reduce error rates, indicating effective noise mitigation. Consequently, PSNR improves with larger qubit sizes, with Q8 consistently achieving the highest fidelity. SSIM values show enhanced structural similarity at higher encoding levels, while degradation is more pronounced in smaller qubit sizes under noisy conditions. UQI trends follow similarly, with perceptual quality improving alongside qubit count and SNR.

In addition to the uncoded scenario, the performance of the channel-coded system is also evaluated under identical HEIF transmission settings, as shown in Figure 8e–h. When classical error correction is applied after decoding the quantum bitstream, all four performance metrics show noticeable gains across all qubit sizes. This further validates the effectiveness of integrating classical channel coding with quantum frequency domain encoding to enhance robustness against noise, especially in practical settings. The comparable results for HEIF and JPEG images indicate that the frequency domain multi-qubit approach, utilizing QFT, ensures scalability and robustness across different image compression schemes in both uncoded and channel-coded environments.

#### 4.5. Time Domain Multi-Qubit Framework for Heif Image Transmission

The performance of the multi-qubit image transmission system in the time domain for HEIF images is evaluated under uncoded and channel coded conditions as shown in Figure 9, complementing the frequency domain results discussed in Section 4.4.

In the uncoded scenario, the BER decreases with increasing SNR across all qubit sizes, as expected; this is shown in Figure 9a. However, the uncoded BER in the time domain is generally higher than in the uncoded frequency domain system, indicating reduced noise robustness. Larger qubit sizes (Q7, Q8) still achieve improved performance but with more noticeable degradation at lower SNRs. PSNR values, as shown in Figure 9b,

increase with SNR and encoding qubit size but remain below those of the frequency domain system, particularly in the low to mid SNR ranges, reflecting more pronounced pixel-level distortions without the frequency domain transformation. The SSIM results in Figure 9c and the UQI results in Figure 9d reveal similar patterns. Both metrics indicate limited structural and perceptual quality at smaller qubit encodings, with noticeable improvements emerging only at higher qubit sizes and SNR levels. These trends emphasize the role of high-dimensional quantum encoding in preserving image quality under noise.

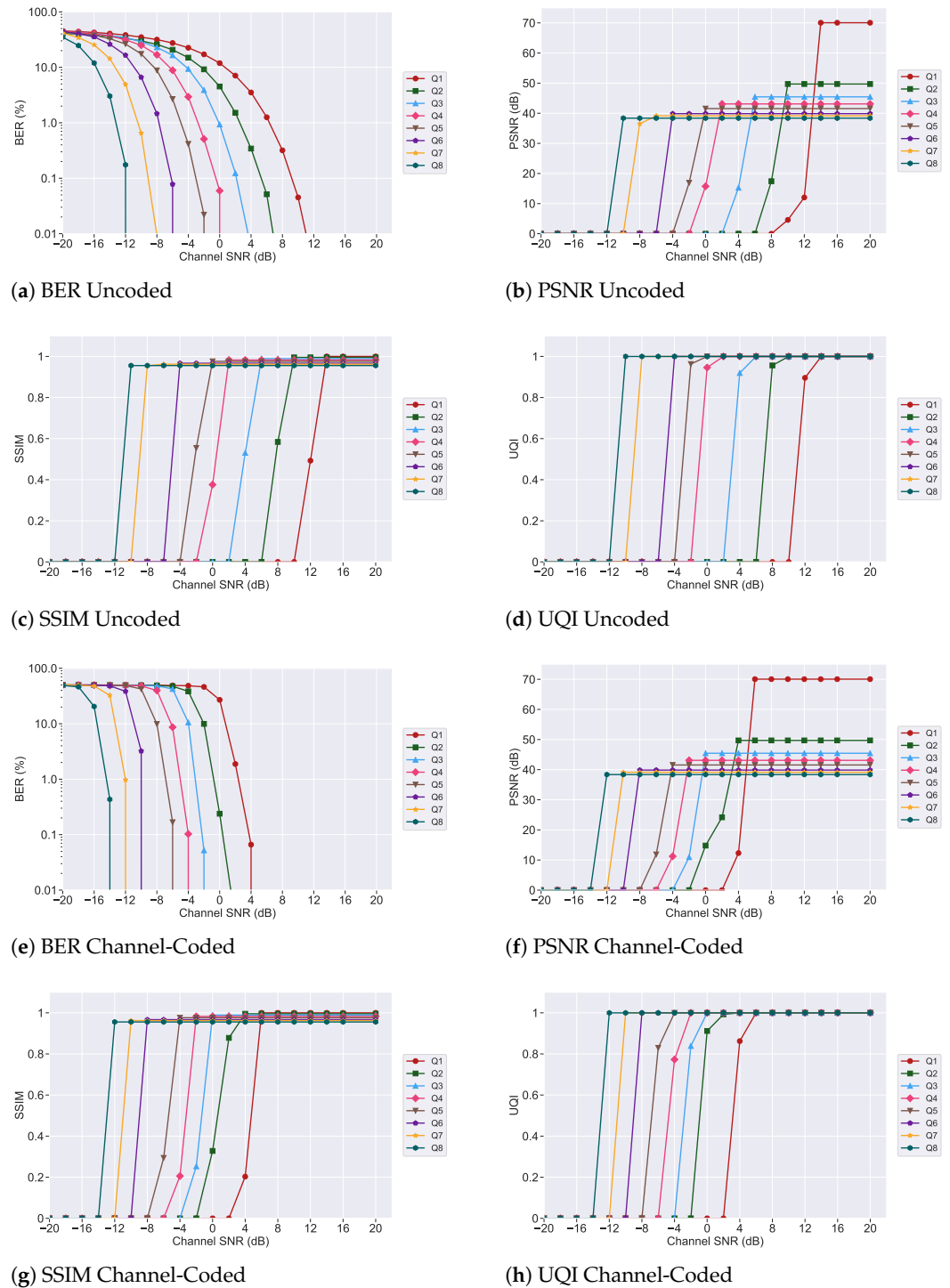


**Figure 8.** Performance evaluation of BER, PSNR, SSIM, and UQI for HEIF images transmitted using frequency domain encoding across varying SNR levels, under both uncoded and channel-coded conditions.

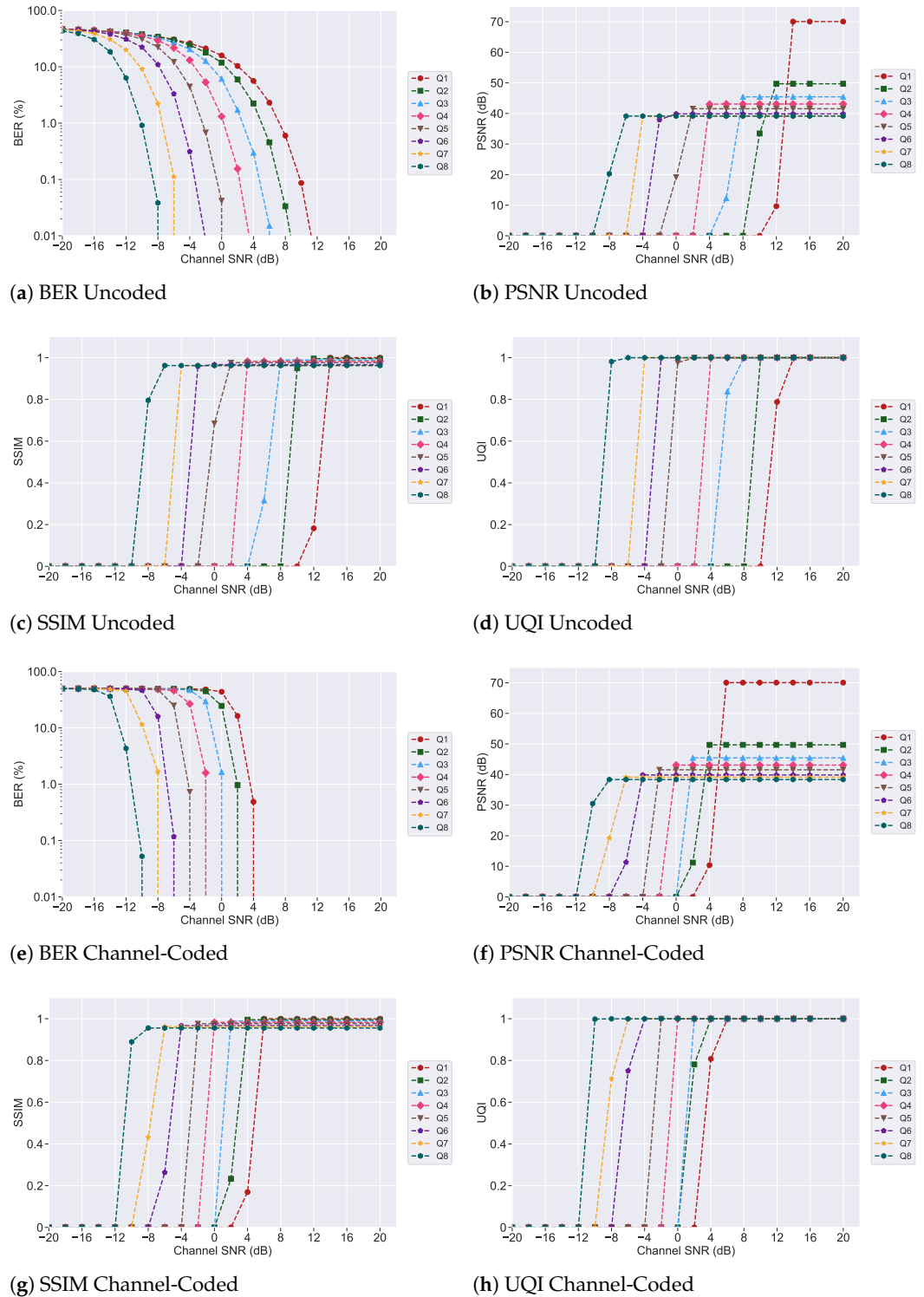


**Figure 9.** Performance evaluation of BER, PSNR, SSIM, and UQI for HEIF images transmitted using time domain encoding across varying SNR levels, under both uncoded and channel-coded conditions.

With the introduction of channel coding, depicted in Figure 9e–h, the performance of the time domain system improves significantly compared to the uncoded scenario. BER significantly drops across all qubit sizes, and even low-qubit encodings achieve reliable transmission at moderate SNRs. PSNR shows considerable gains, indicating effective noise mitigation and better image fidelity, although it still lags slightly behind the frequency domain results. SSIM values rise substantially for qubit sizes Q5 and higher, demonstrating

improved structural integrity supported by classical error correction. UQI values approach unity more rapidly as the SNR and qubit size increase, underscoring enhanced perceptual quality. The Q8 configuration consistently achieves the best performance in all metrics, highlighting the combined benefits of high-dimensional encoding and channel coding. In summary, while the uncoded time domain system is more susceptible to noise, the integration of channel coding significantly improves its robustness and image quality compared to the uncoded scenario.

#### *4.6. Comparing Transmission Efficiency Between Time Domain and Frequency Domain Systems for HEIF Image Transmission*

The comparative evaluation of HEIF image transmission using time domain multi-qubit systems (TQ1 to TQ8) and frequency domain multi-qubit systems (FQ1 to FQ8), shown in Figure 10, reveals distinct performance differences attributable to their respective quantum encoding strategies. Both approaches utilize multi-qubit encoding from Q1 to Q8 to exploit high-dimensional Hilbert spaces and superposition, but the frequency domain system uniquely incorporates additional phase encoding via the QFT. In addition, the time domain system maps classical bitstreams directly into superposition states without phase modulation, limiting its noise distribution capabilities. Consequently, it exhibits higher BER in uncoded scenarios and requires higher SNR for acceptable image quality compared to the frequency domain approach. The QFT stage of the frequency domain system enables energy compaction in fewer dominant components via additional phase encoding, which improves noise robustness. This advantage is evident across all performance metrics in both uncoded and channel-coded cases, with the performance gap especially pronounced at lower SNRs.

Furthermore, similar to JPEG image transmission, the performance difference between time domain and frequency domain encoding remains minimal when using single-qubit systems. This is primarily because the QFT offers limited advantage at such low quantum dimensionality. In single-qubit scenarios, there is insufficient capacity to utilize phase-based encoding or quantum interference, the core strengths of frequency domain techniques. However, as the qubit count increases, frequency domain encoding becomes increasingly beneficial by enabling richer state manipulation and improved error resilience, leading to superior image-reconstruction quality.

It is important to note that single-qubit time domain quantum communication systems have already been shown to outperform classical communication systems, which operate under the same bandwidth constraints using polar coding with a rate of 1/2 and binary phase-shift keying (BPSK) modulation, as demonstrated in Figure 11 for JPEG-compressed images. Furthermore, the comparison is conducted under identical bitrate conditions, and power fairness is ensured by normalizing the energy per bit across both classical and quantum systems at equivalent SNR values. Since these single-qubit systems already exceed classical performance, the proposed frequency domain multi-qubit systems, which provide increased encoding capacity and improved noise resilience, achieve even greater performance improvements over classical methods.

Furthermore, the perceived visual quality of the transmitted images is assessed using a subjective evaluation based on the double stimulus method [57]. A total of 100 participants, aged 18 to 55 years, are involved in the study. JPEG image transmission is used for evaluation across both time domain and frequency domain multi-qubit systems, under both uncoded and channel-coded conditions. For each SNR level, images generated by the quantum systems are presented to the participants, who are asked to rate the visual quality of each image. Ratings are assigned according to the standard mean opinion score (MOS) scale, which ranges from 0 to 100, where 0–20 indicates bad, 21–40 poor, 41–60 fair,

61–80 good, and 81–100 excellent quality. The final MOS values are computed as the average of all participant scores, representing the overall perceived image quality.

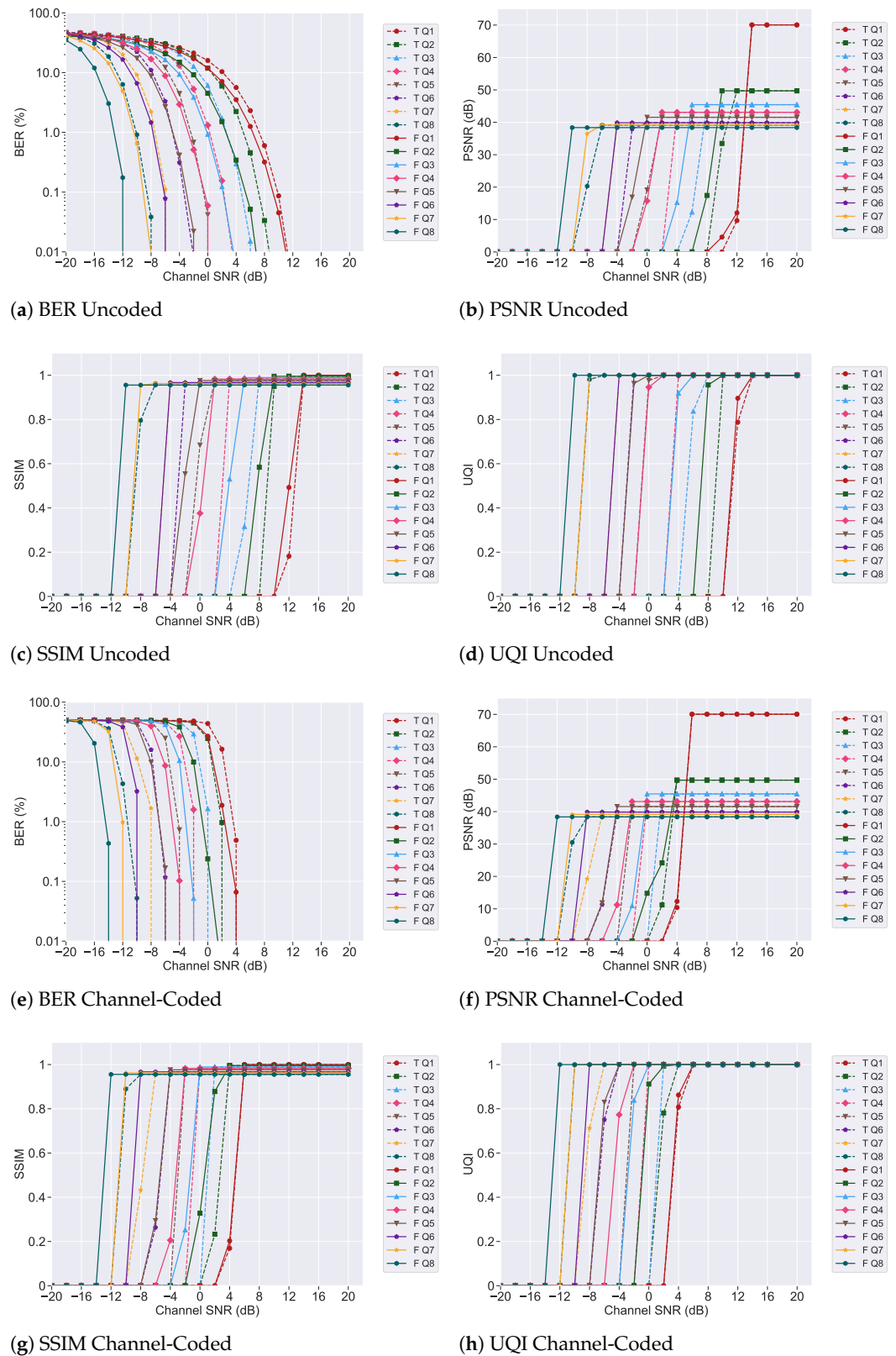


**Figure 10.** Comparative analysis of BER, PSNR, SSIM, and UQI for HEIF image transmission using time domain and frequency domain encoding schemes over varying SNR levels, under both uncoded and channel-coded conditions.

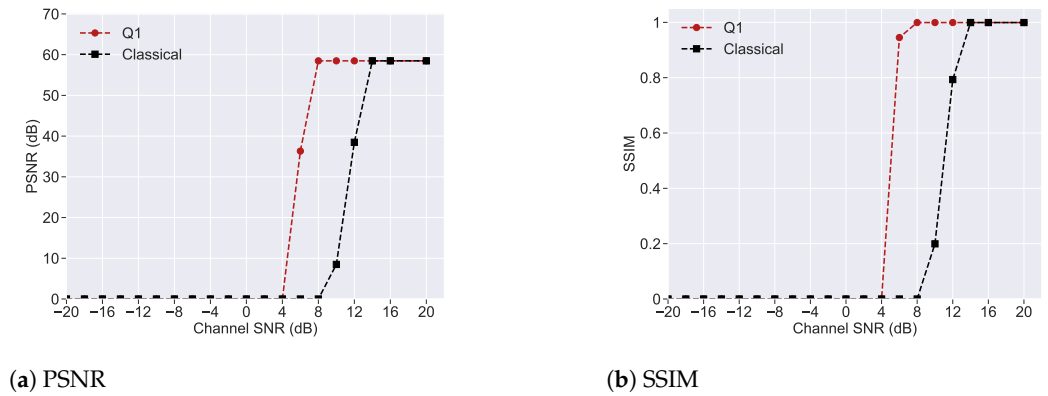


**Figure 11.** Performance comparison between time domain single-qubit quantum system and classical system at the same bandwidth.

Figures 12–15 present the results of this subjective evaluation under four distinct configurations. Figure 12 shows the MOS results for the frequency domain system without channel coding, while Figure 13 displays the frequency domain system with channel coding. Figure 14 illustrates the performance of the time domain system without channel coding, and Figure 15 presents the results of the time domain system with channel coding. These visual comparisons provide information on the impact of both the encoding domain and channel coding on perceived image quality under varying SNR conditions. All subjective results are found to be consistent with the corresponding objective quality metrics, confirming the reliability of the evaluation. Among all configurations, the frequency domain system with channel coding consistently achieves the highest MOS scores, indicating superior visual quality. This suggests that the combination of frequency domain processing and channel coding provides the most effective strategy to preserve image fidelity under noisy channel conditions.

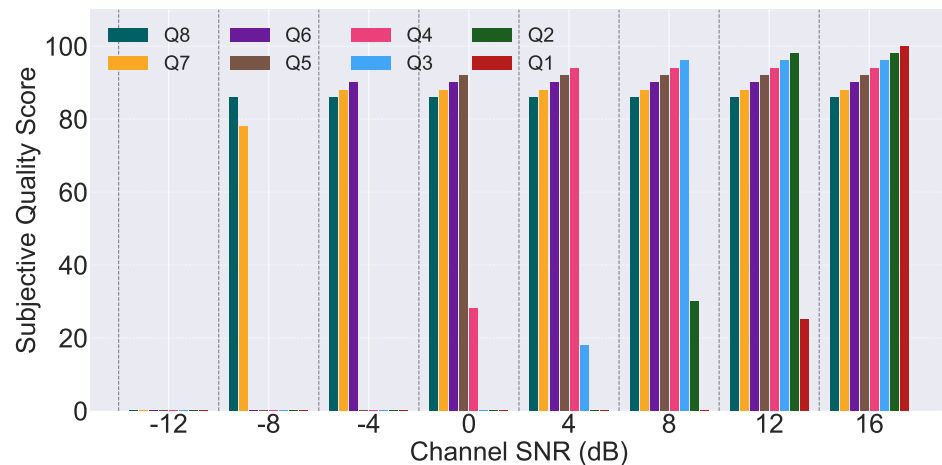


**Figure 12.** Subjective quality assessment results for JPEG image transmission using frequency domain multi-qubit systems under uncoded conditions.

In addition, the analysis of frequency domain and multi-qubit systems indicates that increasing the qubit encoding size from Q1 to Q8 significantly increases system complexity, mainly due to the greater number of quantum gate operations required for both encoding and decoding. As the number of qubits increases, the dimensionality of the Hilbert space expands exponentially, resulting in more intricate superposition states and a greater computational burden on the quantum circuit. Although the Q1 system offers the lowest complexity with minimal quantum gate requirements, it also provides the least resilience to

transmission errors. In contrast, the Q8 system delivers the highest error resilience, but at the cost of substantially increased quantum processing complexity. This illustrates a clear trade-off: higher qubit encoding sizes improve robustness and image quality, but they also demand more computational resources and introduce greater system overhead. Ultimately, the choice of encoding size depends on the desired balance between performance and implementation complexity, with Q1 being suitable for low-complexity scenarios with low noise and Q8 ideal for high-fidelity transmission in high-noise environments with more capable quantum architectures.

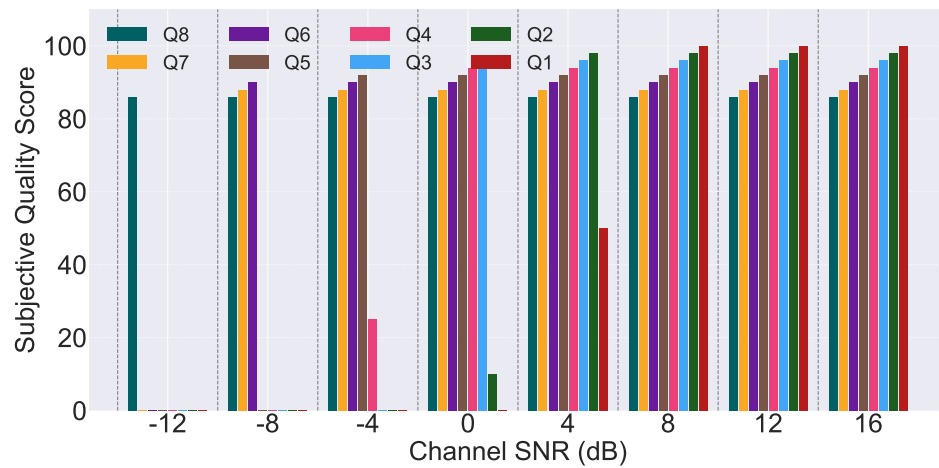


**Figure 13.** Subjective quality assessment results for JPEG image transmission using frequency domain multi-qubit systems under channel-coded conditions.

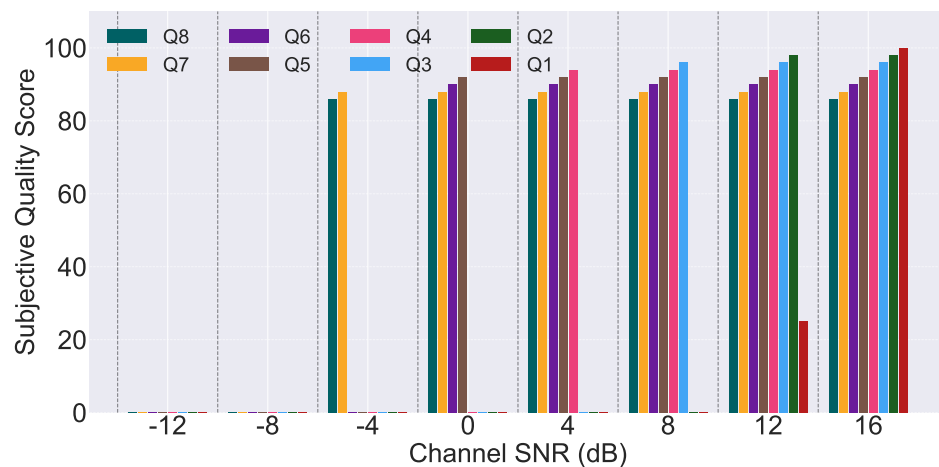


**Figure 14.** Subjective quality assessment results for JPEG image transmission using time domain multi-qubit systems under uncoded conditions.

When comparing the complexity of time domain and frequency domain multi-qubit systems, a key difference emerges in the types and number of quantum gate operations required. The time domain system only uses Hadamard gates to encode classical information into quantum superposition states. These gates are applied independently to each qubit, allowing for full parallelism and resulting in a shallow circuit with low gate complexity. Specifically, the total number of gates scales linearly with the number of qubits, with a gate count of  $n$  and a constant circuit depth of 1, since the encoding is performed using a single-layer transformation. This leads to an overall encoding complexity of  $\mathcal{O}(n)$ , making the time domain system highly efficient and well suited for near-term quantum devices. In contrast, the frequency domain system employs the QFT, which consists of both Hadamard and controlled-phase gates. Due to inter-qubit dependencies, these gates must be applied

sequentially, increasing both the gate count and the circuit depth. For an  $n$ -qubit system, the total number of gates required is  $\frac{n(n+1)}{2}$ , and the circuit depth grows linearly as  $n$ , resulting in an overall complexity of  $\mathcal{O}(n^2)$ .

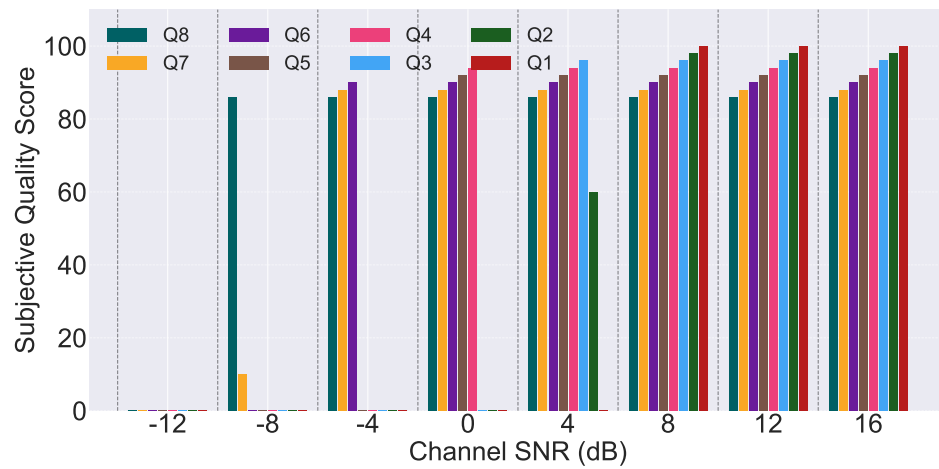


**Figure 15.** Subjective quality assessment results for JPEG image transmission using time domain multi-qubit systems under channel-coded conditions.

Although the frequency domain system introduces greater computational overhead, this added complexity enables more advanced encoding that incorporates both amplitude and phase information. As a result, it offers enhanced noise resistance and superior image fidelity preservation, particularly in challenging transmission environments. Therefore, despite its higher quantum resource demands, the frequency domain approach presents a compelling solution for high-fidelity quantum image communication. A detailed breakdown of gate count, circuit depth, and error resilience for qubit sizes from  $n = 1$  to 8 in both time domain and frequency domain systems is summarized in Table 2.

**Table 2.** Comparison of encoding complexity and error resilience (based on BER at an SNR of  $-8$  dB) for JPEG uncoded images across time domain and frequency domain systems (Q1–Q8).

Qubit Size (n)	Domain	Gate Count	Circuit Depth	BER (%)
Q1	Time	1	1	34.51
Q2	Time	2	1	34.26
Q3	Time	3	1	32.37
Q4	Time	4	1	29.52
Q5	Time	5	1	31.36
Q6	Time	6	1	11.31
Q7	Time	7	1	2.21
Q8	Time	8	1	0.03
Q1	Frequency	1	1	31.56
Q2	Frequency	3	2	26.17
Q3	Frequency	6	3	23.17
Q4	Frequency	10	4	17.36
Q5	Frequency	15	5	8.83
Q6	Frequency	21	6	1.31
Q7	Frequency	28	7	0.02
Q8	Frequency	36	8	0

It is important to note that both systems are suitable for near-term quantum implementations due to their use of simple gates. The time domain system, with its simpler gate requirements and lower circuit depth, is particularly practical for current noisy

intermediate-scale quantum (NISQ) devices, enabling efficient encoding with manageable error accumulation. Meanwhile, despite a higher gate count and increased complexity compared to the time domain system, the frequency domain approach remains implementable on near-term hardware due to ongoing improvements in quantum gate fidelity and error mitigation. The choice between the two depends on the complexity tolerance of the specific application versus the need for enhanced image quality and error resilience. Consequently, the time domain system is particularly suitable for scenarios where implementation simplicity and lower resource consumption are prioritized, such as rapid prototyping, low-complexity quantum communication links, and real-time image streaming in resource-constrained environments. The frequency domain system, on the other hand, is ideal for high-performance quantum image transmission tasks that require superior fidelity and robustness, including secure quantum communications, quantum-enhanced medical imaging, and high-resolution remote sensing.

In addition, quantum error correction (QEC) codes are not used in this study because existing developed QEC methods are highly complex and not compatible with frequency domain error correction. Therefore, a classical error correction is applied after converting the decoded quantum bitstreams back into classical bits. Ultimately, using theoretical validation, our analysis demonstrates the potential of both systems to advance quantum communication technologies. Furthermore, the proposed simulation framework serves as a stepping stone toward realizing practical quantum communication systems for image transmission. Rather than focusing on hardware-specific implementations, the study emphasizes architectural feasibility under generalized noise models, providing a theoretical basis for future physical realizations. By abstracting device-level imperfections, an approach commonly adopted in early-stage quantum research, the work isolates and evaluates the core strengths of the proposed method, including its robustness to noise, efficient bandwidth usage, and low computational complexity. These attributes suggest a strong potential for real-world adaptability, particularly in applications requiring reliable image transmission over constrained or noisy channels. As advancements in quantum hardware accelerate, this framework can inform the design of scalable systems supporting use cases such as remote sensing, medical diagnostics, and real-time communication in resource-limited environments. Although the hybrid classical–quantum structure presents some inherent limitations, it also opens new directions for optimization and integration in future work. Overall, this study sets a firm conceptual and analytical foundation for continued progress in quantum image communication.

## 5. Conclusions and Future Works

This study introduces a novel quantum image transmission framework that leverages frequency domain multi-qubit encoding to significantly enhance robustness and image quality over noisy quantum channels. By integrating advanced source coding methods such as JPEG and HEIF with classical channel coding and multi-qubit quantum encoding, the system effectively balances bandwidth efficiency with error resilience. The use of QFT enables processing in the frequency domain, which offers superior noise immunity compared to traditional techniques in the time domain. A key advantage of the frequency domain approach is its exploitation of a higher-dimensional Hilbert space, not only through quantum state superposition, as in time domain encoding, but also via additional phase encoding introduced by the QFT. This enhanced quantum state representation facilitates improved error resilience and increased information capacity, positioning frequency domain encoding as a highly promising strategy for achieving high-fidelity quantum multimedia transmission.

Evaluation based on BER, PSNR, SSIM, and UQI metrics shows that increasing the number of qubits consistently improves image reconstruction quality and noise resilience in both time and frequency domains, albeit at the cost of increased system complexity. Larger qubit encoding sizes enable more expressive quantum state representations, but the computational and physical resource demands also increase. Notably, frequency domain encoding achieves significant performance gains of up to 4 dB in channel SNR, especially for eight-qubit configurations, in both JPEG and HEIF image formats compared to time domain systems. In contrast, the single-qubit system shows only a modest performance gap between time and frequency domain encoding, reflecting its limited capacity to harness the advantages offered by frequency domain processing. Overall, the frequency domain multi-qubit framework offers an effective trade-off between complexity and performance and is a promising solution for high-fidelity quantum image transmission.

Future research will focus on designing an adaptive frequency domain multi-qubit system that balances image quality and system complexity. To achieve this, machine learning techniques such as reinforcement learning (RL) will be explored to enable intelligent and dynamic control of qubit encoding sizes. In this framework, the qubit-size selection problem will be formulated as a sequential decision-making process, where an RL agent interacts with a quantum channel environment and learns to adapt encoding strategies based on real-time channel state information (CSI) to maximize transmission performance. A low-complexity QEC scheme tailored for frequency domain multi-qubit systems will also be developed, removing the reliance on traditional high-complexity QEC codes. To further reduce gate overhead, optimized implementations of the QFT, such as approximate QFT (AQFT), will be investigated to maintain fidelity while minimizing circuit depth, particularly for systems with higher qubit counts. Finally, the proposed framework will be extended and evaluated for quantum video transmission, with performance analyzed in terms of fidelity, compression efficiency, and robustness under dynamic and noisy quantum communication conditions.

**Author Contributions:** Conceptualization, U.J.; methodology, U.J.; software, U.J. and T.F.; validation, U.J. and A.F.; formal analysis, A.F.; investigation, A.F.; resources, U.J.; data curation, U.J.; writing—original draft preparation, U.J.; writing—review and editing, T.F.; visualization, U.J.; supervision, A.F.; project administration, A.F. All authors have read and agreed to the published version of the manuscript.

**Funding:** This research received no external funding.

**Data Availability Statement:** The original data presented in the study are openly available in the Microsoft COCO dataset at <https://cocodataset.org>.

**Conflicts of Interest:** The authors declare no conflicts of interest.

## Abbreviations

AQFT	Approximate QFT
AR	Augmented Reality
BER	Bit Error Rate
CSI	Channel State Information
HEIF	High Efficiency Image Format
IQFT	Inverse Quantum Fourier Transform
JPEG	Joint Photographic Experts Group
LDPC	Low-Density Parity-Check
MOS	Mean Opinion Score
NISQ	Noisy Intermediate Scale Quantum
PSNR	Peak Signal-to-Noise Ratio

QEC	Quantum Error Correction
QFT	Multi-Input Single-Output
QKD	Quantum Key Distribution
RL	Reinforcement Learning
SI	Spatial Information
SNR	Signal-to-Noise Ratio
SSIM	Structural Similarity Index Measure
UQI	Universal Quality Index

## References

1. Arena, F.; Collotta, M.; Pau, G.; Termine, F. An Overview of Augmented Reality. *Computers* **2022**, *11*, 28. [[CrossRef](#)]
2. Shannon, C.E.; Weaver, W. *The Mathematical Theory of Communication*; University of Illinois Press: Urbana, IL, USA, 1949.
3. Arun, G.; Mishra, V. A review on quantum computing and communication. In Proceedings of the 2014 2nd International Conference on Emerging Technology Trends in Electronics, Communication and Networking, Surat, India, 26–27 December 2014; pp. 1–5. [[CrossRef](#)]
4. Yasmineh, S. Foundations of Quantum Mechanics. *Encyclopedia* **2022**, *2*, 1082–1090. [[CrossRef](#)]
5. Ralston, J. What Can We Learn from Entanglement and Quantum Tomography? *Physics* **2022**, *4*, 1371–1383. [[CrossRef](#)]
6. Jayasinghe, U.; Samarathunga, P.; Ganearachchi, Y.; Fernando, T.; Fernando, A. Quantum communications for image transmission over error-prone channels. *Electron. Lett.* **2024**, *60*, e13300. [[CrossRef](#)]
7. Camps, D.; Van Beeumen, R.; Yang, C. Quantum Fourier transform revisited. *Numer. Linear Algebra Appl.* **2021**, *28*, e2331. [[CrossRef](#)]
8. Ballentine, L.E. *Quantum Mechanics: A Modern Development*, 2nd ed.; World Scientific Publishing Company: Singapore, 2014; p. 740.
9. Sridhar, G.T.; Ashwini, P.; Tabassum, N. A Review on Quantum Communication and Computing. In Proceedings of the 2023 2nd International Conference on Applied Artificial Intelligence and Computing (ICAAIC), Salem, India, 4–6 May 2023; pp. 1592–1596. [[CrossRef](#)]
10. Hughes, C.; Isaacson, J.; Perry, A.; Sun, R.F.; Turner, J. Introduction to Superposition. In *Quantum Computing for the Quantum Curious*; Springer International Publishing: Berlin/Heidelberg, Germany, 2021; pp. 1–5. [[CrossRef](#)]
11. Zou, N. Quantum Entanglement and Its Application in Quantum Communication. *J. Physics Conf. Ser.* **2021**, *1827*, 012120. [[CrossRef](#)]
12. Tao, Y. Quantum entanglement: Principles and research progress in quantum information processing. *Theor. Nat. Sci.* **2024**, *30*, 263–274. [[CrossRef](#)]
13. Sehgal, S.K.; Gupta, R. Quantum Cryptography and Quantum Key. In Proceedings of the 2021 International Conference on Industrial Electronics Research and Applications (ICIARA), New Delhi, India, 22–24 December 2021; pp. 1–5. [[CrossRef](#)]
14. Durr-E-Shahwar; Imran, M.; Altamimi, A.B.; Khan, W.; Hussain, S.; Alsaffar, M. Quantum Cryptography for Future Networks Security: A Systematic Review. *IEEE Access* **2024**, *12*, 180048–180078. [[CrossRef](#)]
15. Wang, P.; Zhang, X.; Chen, G. Efficient quantum-error correction for QoS provisioning over QKD-based satellite networks. In Proceedings of the 2015 IEEE Wireless Communications and Networking Conference (WCNC), New Orleans, LA, USA, 9–12 March 2015; pp. 2262–2267. [[CrossRef](#)]
16. Comi, P.; Martelli, P.; Martin, V.; Brito, J.P.; Gatto, A.; Méndez, R.B.; Vicente, R.J.; Bianchi, F.; Brunero, M. Increasing network reliability by securing SDN communication with QKD. In Proceedings of the 2021 17th International Conference on the Design of Reliable Communication Networks (DRCN), Milano, Italy, 19–22 April 2021; pp. 1–3. [[CrossRef](#)]
17. Mamiya, A.; Tanaka, K.; Yokote, S.; Sasaki, M.; Fujiwara, M.; Tanaka, M.; Sato, H.; Katagiri, Y. Satellite-based QKD for Global Quantum Cryptographic Network Construction. In Proceedings of the 2022 IEEE International Conference on Space Optical Systems and Applications (ICSOS), Kyoto City, Japan, 28–31 March 2022; pp. 47–50. [[CrossRef](#)]
18. Karthik, M.; Lalwani, J.; Jajodia, B. Quantum Image Teleportation Protocol (QITP) and Quantum Audio Teleportation Protocol (QATP) by using Quantum Teleportation and Huffman Coding. In Proceedings of the 2022 International Conference on Trends in Quantum Computing and Emerging Business Technologies (TQCEBT), Pune, India, 13–15 October 2022; pp. 1–6. [[CrossRef](#)]
19. Tan, X.; Jiang, L.; Zhang, Q. Controlled Quantum Teleportation with Identity Authentication. In Proceedings of the 2013 Fourth International Conference on Emerging Intelligent Data and Web Technologies, Xi'an, China, 9–11 September 2013; pp. 350–355. [[CrossRef](#)]
20. Janani, T.; Brindha, M. A secure medical image transmission scheme aided by quantum representation. *J. Inf. Secur. Appl.* **2021**, *59*, 102832. [[CrossRef](#)]

21. Yamaguchi, T.; Kimura, N.; Mochida, Y.; Mizuno, K.; Takasugi, K.; Chikara, S.; Saito, T.; Shirai, D. Uncompressed 8K-video-transmission System for Remote Production Secured by Post-quantum Cryptography. In Proceedings of the 2023 IEEE International Symposium on Broadband Multimedia Systems and Broadcasting (BMSB), Beijing, China, 14–16 June 2023; pp. 1–6. [[CrossRef](#)]
22. Guérin, P.A.; Feix, A.; Araújo, M.; Brukner, I.C.V. Exponential Communication Complexity Advantage from Quantum Superposition of the Direction of Communication. *Phys. Rev. Lett.* **2016**, *117*, 100502. [[CrossRef](#)]
23. Feix, A.; Araújo, M.; Brukner, i.c.v. Quantum superposition of the order of parties as a communication resource. *Phys. Rev. A* **2015**, *92*, 052326. [[CrossRef](#)]
24. Goswami, K.; Cao, Y.; Paz-Silva, G.A.; Romero, J.; White, A.G. Increasing communication capacity via superposition of order. *Phys. Rev. Res.* **2020**, *2*, 033292. [[CrossRef](#)]
25. Guo, Y.; Hu, X.M.; Hou, Z.B.; Cao, H.; Cui, J.M.; Liu, B.H.; Huang, Y.F.; Li, C.F.; Guo, G.C.; Chiribella, G. Experimental Transmission of Quantum Information Using a Superposition of Causal Orders. *Phys. Rev. Lett.* **2020**, *124*, 030502. [[CrossRef](#)]
26. Jayasinghe, U.; Samarathunga, P.; Ganearachchi, Y.; Fernando, T.; Fernando, A. Adaptive Coding-Based Quantum Communication System for Image Transmission. *Electron. Lett.* **2025**, *61*, e70299. [[CrossRef](#)]
27. Jayasinghe, U.; Pollwaththage, N.; Ganearachchi, Y.; Samarathunga, P.; Fernando, T.; Fernando, A. Quantum Communication based Image Transmission over Error-Prone Channels with Three-Qubit Stabilizer Code. In Proceedings of the 2025 IEEE International Conference on Consumer Electronics (ICCE), Las Vegas, NV, USA, 11–14 January 2025; pp. 1–6. [[CrossRef](#)]
28. Jayasinghe, U.; Samarathunga, P.; Pollwaththage, N.; Ganearachchi, Y.; Fernando, T.; Fernando, A. Quantum Communication for Video Transmission Over Error-Prone Channels. *IEEE Trans. Consum. Electron.* **2025**, *71*, 1148–1155. [[CrossRef](#)]
29. Jayasinghe, U.; Fernando, T.; Ganearachchi, Y.; Samarathunga, P.; Fernando, A. Quantum Communication Based Image Transmission with Transmit and Receive Diversity in MIMO Communication Systems. *IEEE Trans. Consum. Electron.* **2025**, *1*. [[CrossRef](#)]
30. Singamaneni, K.K.; Muhammad, G.; Ali, Z. A Novel Multi-Qubit Quantum Key Distribution Ciphertext-Policy Attribute-Based Encryption Model to Improve Cloud Security for Consumers. *IEEE Trans. Consum. Electron.* **2024**, *70*, 1092–1101. [[CrossRef](#)]
31. Pan, H. Multi-party semiquantum key distribution with multi-qubit GHZ states. *Quantum Inf. Process.* **2024**, *23*, 1–17. [[CrossRef](#)]
32. Zhou, T.; Chen, X.B.; Xu, G.; Guo, Y.; Li, Z. Multi-qubit hierarchical quantum state sharing with authentication. *Quantum Inf. Process.* **2025**, *24*, 69. [[CrossRef](#)]
33. Espoukeh, P.; Pedram, P. Quantum teleportation through noisy channels with multi-qubit GHZ states. *Quantum Inf. Process.* **2014**, *13*, 1789–1811. [[CrossRef](#)]
34. Yi, Y.H.; Li, X.L.; Nie, L.P.; Sang, M.H. Quantum Teleportation of Three and Four-Qubit State Using Multi-qubit Cluster States. *Int. J. Theor. Phys.* **2016**, *55*, 1820–1823. [[CrossRef](#)]
35. Zhou, S.S.; Loke, T.; Izaac, J.A.; Wang, J.B. Quantum Fourier transform in computational basis. *Quantum Inf. Process.* **2017**, *16*, 82. [[CrossRef](#)]
36. Amankwah, M.G.; Camps, D.; Bethel, E.W.; Jones, M.W.; Martinez-Rach, M.A.; Uelwer, T.; Cruz, C.D.; Blanes, I.; Artés, A.; Bernardos, A.M. Quantum pixel representations and compression for N-dimensional images. *Sci. Rep.* **2022**, *12*, 7712. [[CrossRef](#)]
37. Haque, M.E.; Paul, M.; Ulhaq, A.; Debnath, T. Advanced quantum image representation and compression using a DCT-EFRQI approach. *Sci. Rep.* **2023**, *13*, 4129. [[CrossRef](#)] [[PubMed](#)]
38. Devarapalli, S.H.R.; Jadhav, H.; Dontabhaktuni, J. Image compression using quantum wavelet transforms. *Proc. SPIE Int. Soc. Opt. Eng.* **2025**, *13391*, 1339117. [[CrossRef](#)]
39. Ma, Y.; Zhou, N. Quantum color image compression and encryption algorithm based on Fibonacci transform. *Quantum Inf. Process.* **2023**, *22*, 39. [[CrossRef](#)]
40. Wang, H.; Tan, J.; Huang, Y.; Zheng, W. Quantum image compression with autoencoders based on parameterized quantum circuits. *Quantum Inf. Process.* **2024**, *23*, 41. [[CrossRef](#)]
41. Mukhamedieva, D.T.; Sobirov, R.A.; Turg'unova, N.; Samijonov, B.N. Quantum Fourier Transform in Image Processing. In *Information Technologies and Intelligent Decision Making Systems; Communications in Computer and Information Science*; Springer: Berlin/Heidelberg, Germany, 2024; pp. 143–151. [[CrossRef](#)]
42. Yan, X.Y.; Zhou, N.R.; Gong, L.H.; Wang, Y.Q.; Wen, X.J. High-dimensional quantum key distribution based on qudits transmission with quantum Fourier transform. *Quantum Inf. Process.* **2019**, *18*, 271. [[CrossRef](#)]
43. Song, D.; He, C.; Cao, Z.; Chai, G. Quantum Teleportation of Multiple Qubits Based on Quantum Fourier Transform. *IEEE Commun. Lett.* **2018**, *22*, 2427–2430. [[CrossRef](#)]
44. Mastriani, M. Quantum Fourier states and gates: Teleportation via rough entanglement. *Opt. Quantum Electron.* **2023**, *55*, 1111. [[CrossRef](#)]
45. Cao, Z.; Zhang, C.; He, C.; Zhang, M. Quantum Teleportation Protocol of Arbitrary Quantum States by Using Quantum Fourier Transform. *Int. J. Theor. Phys.* **2020**, *59*, 3174–3183. [[CrossRef](#)]

46. Jayasinghe, U.; Samarathunga, P.; Fernando, T.; Ganearachchi, Y.; Fernando, A. Image Transmission Over Quantum Communication Systems With Three-Qubit Error Correction. *Electron. Lett.* **2025**, *61*, e70205. [[CrossRef](#)]
47. Jayasinghe, U.; Samarathunga, P.; Fernando, T.; Fernando, A. Transmit and Receive Diversity in MIMO Quantum Communication for High-Fidelity Video Transmission. *Algorithms* **2025**, *18*, 436. [[CrossRef](#)]
48. Johnson, S.; Rarity, J.; Padgett, M. Transmission of quantum-secured images. *Sci. Rep.* **2024**, *14*, 11579. [[CrossRef](#)]
49. Lin, T.Y.; Maire, M.; Belongie, S.; Hays, J.; Perona, P.; Ramanan, D.; Dollár, P.; Zitnick, C.L. Microsoft COCO: Common Objects in Context. In *Proceedings of the Computer Vision—ECCV 2014*; Lecture Notes in Computer Science; Springer: Cham, Switzerland, 2014; Volume 8693, pp. 740–755. [[CrossRef](#)]
50. Wallace, G. The JPEG still picture compression standard. *IEEE Trans. Consum. Electron.* **1992**, *38*, xviii–xxxiv. [[CrossRef](#)]
51. Hannuksela, M.M.; Lainema, J.; Malamal Vadakital, V.K. The High Efficiency Image File Format Standard [Standards in a Nutshell]. *IEEE Signal Process. Mag.* **2015**, *32*, 150–156. [[CrossRef](#)]
52. Pathak, P.; Bhatia, R. Performance analysis of Polar codes for next generation 5G technology. In *Proceedings of the 2022 3rd International Conference for Emerging Technology (INCET)*, Belgaum, India, 27–29 May 2022; pp. 1–4. [[CrossRef](#)]
53. Nielsen, M.A.; Chuang, I.L. *Quantum Computation and Quantum Information: 10th Anniversary Edition*; Cambridge University Press: Cambridge, UK, 2010.
54. Chakraborty, M.; Mukherjee, A.; Nag, A.; Chandra, S. Hybrid Quantum Noise Model to Compute Gaussian Quantum Channel Capacity. *IEEE Access* **2024**, *12*, 14671–14689. [[CrossRef](#)]
55. Wille, R.; Lye, A.; Drechsler, R. Optimal SWAP gate insertion for nearest neighbor quantum circuits. In *Proceedings of the 2014 19th Asia and South Pacific Design Automation Conference (ASP-DAC)*, Singapore, 20–23 January 2014; pp. 489–494. [[CrossRef](#)]
56. Dixit, V.; Jian, S. Quantum Fourier transform to estimate drive cycles. *Sci. Rep.* **2022**, *12*, 654. [[CrossRef](#)] [[PubMed](#)]
57. International Telecommunication Union (ITU). *Methodologies for the Subjective Assessment of the Quality of Television Pictures*; ITU-R Recommendation BT.500; International Telecommunication Union: Geneva, Switzerland, 2022.

**Disclaimer/Publisher’s Note:** The statements, opinions and data contained in all publications are solely those of the individual author(s) and contributor(s) and not of MDPI and/or the editor(s). MDPI and/or the editor(s) disclaim responsibility for any injury to people or property resulting from any ideas, methods, instructions or products referred to in the content.